



HAL
open science

High-P metamorphism of rodingites during serpentinite dehydration (Cerro del Almirez, Southern Spain): Implications for the redox state in subduction zones

Casto Laborda-Lopez, Vicente Lopez-Sanchez-Vizcaino, Claudio Marchesi, Maria T. Gomez-Pugnaire, Carlos J. Garrido, Antonio Jabaloy-Sanchez, Jose Alberto Padron Navarta, Karoly Hidas

► To cite this version:

Casto Laborda-Lopez, Vicente Lopez-Sanchez-Vizcaino, Claudio Marchesi, Maria T. Gomez-Pugnaire, Carlos J. Garrido, et al.. High-P metamorphism of rodingites during serpentinite dehydration (Cerro del Almirez, Southern Spain): Implications for the redox state in subduction zones. *Journal of Metamorphic Geology*, 2018, 36 (9), pp.1141-1173. 10.1111/jmg.12440 . hal-01983584

HAL Id: hal-01983584

<https://hal.science/hal-01983584>

Submitted on 2 Sep 2021

HAL is a multi-disciplinary open access archive for the deposit and dissemination of scientific research documents, whether they are published or not. The documents may come from teaching and research institutions in France or abroad, or from public or private research centers.

L'archive ouverte pluridisciplinaire **HAL**, est destinée au dépôt et à la diffusion de documents scientifiques de niveau recherche, publiés ou non, émanant des établissements d'enseignement et de recherche français ou étrangers, des laboratoires publics ou privés.



Distributed under a Creative Commons Attribution 4.0 International License

High-*P* metamorphism of rodingites during serpentinite dehydration (Cerro del Almirez, Southern Spain): Implications for the redox state in subduction zones

Casto Laborda-López¹  | Vicente López-Sánchez-Vizcaíno¹ | Claudio Marchesi^{2,3} |
 María T. Gómez-Pugnaire^{2,3} | Carlos J. Garrido² | Antonio Jabaloy-Sánchez⁴ |
 José A. Padrón-Navarta⁵ | Károly Hidas²

¹Departamento de Geología (Unidad Asociada al IACT-CSIC), Universidad de Jaén, Linares, Spain

²Instituto Andaluz de Ciencias de la Tierra, CSIC-Universidad de Granada, Armilla (Granada), Spain

³Departamento de Mineralogía y Petrología, Universidad de Granada, Granada, Spain

⁴Departamento de Geodinámica, Universidad de Granada, Granada, Spain

⁵Géosciences Montpellier, UMR 5243, CNRS-Université de Montpellier, Montpellier, France

Correspondence

Casto Laborda-López, Departamento de Geología (Unidad Asociada al IACT-CSIC), Universidad de Jaén, Linares, Spain.

Email: claborda@ujaen.es

Funding information

“Ministerio de Economía, Industria y Competitividad” (MINECO), Grant/Award Number: CGL2012-32067, CGL2016-75224-R; Junta de Andalucía, Grant/Award Number: RNM-145, P12-RNM-3141; Ramón y Cajal, Grant/Award Number: RYC-2012-11314; MINECO, Grant/Award Number: CGL2016-81085-R, PCIN-2015-053

Handling Editor: Doug Robinson

Abstract

The transition between antigorite-serpentinite and chlorite-harzburgite at Cerro del Almirez (Betic Cordillera, Southern Spain) exceptionally marks in the field the front of antigorite breakdown at high pressure (~16–19 kbar) and temperature (~650°C) in a paleosubducted serpentinite. These ultramafic lithologies enclose three types of metaroddingite boudins of variable size surrounded by metasomatic reaction rims. Type 1 Grandite-metaroddingite (garnet+chlorite+diopside+titanite±magnetite±ilmenite) mainly crops out in the antigorite-serpentinite domain and has three generations of garnet. Grossular-rich Grt-1 formed during rodingitization at the seafloor (<2 kbar, ~150–325°C, ~FMQ buffer). During subduction, the alternating growth of Grt-2b (richer in andradite and pyralpsite components than Grt-1) and Grt-3 (very rich in andradite component) reflects the change from internally buffered metamorphic conditions (>10 kbar, ~350–650°C, ~FMQ buffer) to influx events of oxidizing fluids (fO_2 ~HM buffer) released by brucite breakdown in the host antigorite-serpentinite. Type 2 Epidote-metaroddingite (epidote+diopside+titanite±garnet) derives from Type 1 and is the most abundant metaroddingite type enclosed in dehydrated chlorite-harzburgite. Type 2 formed by increasing μSiO_2 (from –884 to –860 kJ/mol) and decreasing μCaO (from –708 to –725 kJ/mol) triggered by the flux of high amounts of oxidizing fluids during the high-*P* antigorite breakdown in serpentinite. The growth of Grt-4, with low-grandite and high-pyralpsite components, in Type 2 metaroddingite accounts for progressive reequilibration of garnet with changing intensive variables. Type 3 Pyralpsite-metaroddingite (garnet+epidote+amphibole+chlorite±diopside+rutile) crops out in the chlorite-harzburgite domain and formed at peak metamorphic conditions (16–19 kbar, 660–684°C) from Type 2 metaroddingite. This transformation caused the growth of a last generation of pyralpsite-rich garnet (Grt-5) and the recrystallization of diopside into tremolitic amphibole at decreasing fO_2 and μCaO (from –726 to –735 kJ/mol) and increasing μMgO (from –630 to –626 kJ/mol) due to chemical mixing between the metaroddingite and the reaction

This is an open access article under the terms of the Creative Commons Attribution License, which permits use, distribution and reproduction in any medium, provided the original work is properly cited.

© 2018 The Authors. *Journal of Metamorphic Geology* Published by John Wiley & Sons Ltd

rims. The different bulk $\text{Fe}^{3+}/\text{Fe}_{\text{Total}}$ ratios of antigorite-serpentinite and chlorite-harzburgite, and of the three metarodingite types, reflect the highly heterogeneous oxidation state of the subducting slab and likely point to the transfer of localized oxidized reservoirs, such as metarodingites, into the deep mantle.

KEYWORDS

Cerro del Almirez, oxygen fugacity, rodingite, serpentinite dehydration, subduction

1 | INTRODUCTION

Rodingites are CaO-rich, SiO_2 -, Na_2O -, and K_2O -poor rocks formed by metasomatic alteration (rodingitization) of mainly gabbros and basalts. They mostly consist of Ca-Al and Ca-Mg silicates and occur as dykes or boudins (<10 cm to several metres thick) included in serpentinitized peridotites (e.g., Bach & Klein, 2009; Coleman, 1967; Frost, 1975). Since their first description by Bell, Clarke, and Marshall (1911), and Benson (1913, Part I), rodingites have been documented in a range of tectonic settings, including active seafloor spreading centres (Aumento & Loubat, 1971; Frost, Beard, McCaig, & Condliffe, 2008; Früh-Green et al., 2017; Honnorez & Kirst, 1975), rifted continental margins (Beard, Fullagar, & Krishna Sinha, 2002), greenstone belts (Anhaeusser, 1979; Attoh, Evans, & Bickford, 2006; Schandl, O'Hanley, & Wicks, 1989), and Phanerozoic orogenic belts (Austrheim & Prestvik, 2008; Coleman, 1967; Dubinska, 1995; Evans, Trommsdorff, & Richter, 1979; Frost, 1975; Hatzipanagiotou & Tsikouras, 2001; Li, Rahn, & Bucher, 2004; Li, Zhang, Wei, Ai, & Chen, 2007; Murzin & Shanina, 2007; Tsikouras et al., 2009; Zaroni, Rebay, & Spalla, 2016).

Rodingitization of mafic igneous rocks and serpentinization of their host ultramafic rocks take place simultaneously on the seafloor (e.g., Arshinov & Merenkov, 1930; Coleman, 1967; Frost, 1975; O'Hanley, Schandl, & Wicks, 1992; Schandl, O'Hanley, Wicks, & Kyser, 1990; Suzuki, 1954). Rarely, rodingites form during serpentinization of Archean komatiites (Mogessie & Rammlair, 1994; Schandl et al., 1989), in the mantle wedge above a subducting slab (Koutsovitis, Magganas, Pomonis, & Ntaflos, 2013), or through exhumation of slab eclogites (Li et al., 2007). During rodingitization, Ca-rich and Si-undersaturated fluids (Bach & Klein, 2009; Coleman, 1967; Frost & Beard, 2007; Li et al., 2004) react with igneous mafic rocks, sometimes in different stages (e.g., Normand & Williams-Jones, 2007; Schandl et al., 1989), leading to depletion of Na, K, and Si.

Most petrological studies on metamorphosed rodingites (metarodingites) focus on their tectonometamorphic evolution based on their stable mineral assemblages and associated textures. In some of these investigations, mineralogical variations between different metarodingite types have been attributed to different degrees of oceanic metasomatism that

were preserved during subsequent metamorphism (e.g., Ferrando, Frezzotti, Orione, Conte, & Compagnoni, 2010; Li et al., 2004). However, only a few studies have precisely determined the metamorphic evolution of metarodingites by detailed thermodynamic modelling (e.g., Li, Rahn, & Bucher, 2008; Li et al., 2017; Zaroni et al., 2016).

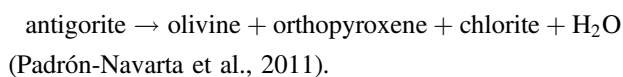
The mineralogical and compositional changes produced in metarodingites by interaction with enclosing serpentinites have only seldom been dealt with (Li et al., 2004). Except for the Cima di Gagnone locality, where metarodingites are hosted by chlorite-harzburgite (Evans et al., 1979) formed after antigorite-serpentinite dehydration (Evans & Trommsdorff, 1978), all other metarodingite studies have examined rocks hosted by serpentinites, in which antigorite (e.g., Panzeri, Fontana, & Tartarotti, 2008; and references therein; Zaroni et al., 2016) but also chrysotile and lizardite (Coleman, 1967; Lan & Liou, 1981) were stable. That precluded the possibility to study the interaction between metarodingites and the fluids released during antigorite breakdown.

In this work, we describe the main structural, mineralogical, textural, and compositional features of metarodingites from Cerro del Almirez (Betic Cordillera, southern Spain) and present a detailed thermodynamic model of their metamorphic evolution during subduction. The Cerro del Almirez ultramafic massif is a unique location where metarodingite bodies occur on both sides of the antigorite-out isograd mapped in their host ultramafic rocks (Trommsdorff, López-Sánchez-Vizcaíno, Gomez-Pugnaire, & Müntener, 1998). The breakdown of antigorite in serpentinite is the main dehydration reaction occurring at high pressure in subduction zones (Padrón-Navarta, Tommasi, et al., 2010; Ulmer & Trommsdorff, 1995). Owing to serpentinite dehydration, oxidizing fluids are released (Debret & Sverjensky, 2017; Debret et al., 2014, 2015; Merkulova et al., 2017) and may interact with subducted lithologies, including metarodingites, inducing mineralogical and/or compositional changes in rocks and fluids. Therefore, metarodingites from Cerro del Almirez are ideal for unravelling how fluids from dehydration reactions may trigger metamorphic/metasomatic reactions in subducted mafic rocks, and how these reactions affect the compositions of the slab recycled deep in the mantle and of fluids that migrate to inner regions of the mantle wedge where arc magmas are generated.

2 | GEOLOGICAL SETTING

The Cerro del Almiraz ultramafic massif is the largest (~2.3 km² and 0.4 km thick) of several ultramafic bodies that crop out in the upper lithological sequence of the Nevado-Filábride Complex, the lowermost tectono-metamorphic unit of the Internal Zones of the Betic Cordillera (Figure 1a). The Nevado-Filábride Complex mainly consists of metasedimentary rocks locally intercalated with metagranites, eclogites, amphibolites and serpentinites (Gómez-Pugnaire et al., 2012; and references therein). This complex likely represents the subducted paleomargin of the Iberian Variscan Massif (Booth-Rea, Ranero, Martínez-Martínez, & Grevemeyer, 2007; Gómez-Pugnaire et al., 2012). Peak eclogite facies conditions were reached during Alpine subduction in the middle Miocene (Kirchner, Behr, Loewy, & Stockli, 2016; López-Sánchez-Vizcaíno, Rubatto, Gómez-Pugnaire, Trommsdorff, & Müntener, 2001; Platt, Anczkiewicz, Soto, Kelley, & Thirlwall, 2006), followed by retrogression at amphibolite or greenschist facies conditions during exhumation (Bakker, Jong, Helmers, & Biermann, 1989; Behr & Platt, 2012; Gómez-Pugnaire & Fernández-Soler, 1987).

In the Cerro del Almiraz massif, two main ultramafic lithologies occur: antigorite-serpentinite (hereafter Atg-serpentinite) and chlorite-harzburgite (Chl-harzburgite), which are separated by ~1 m thick transitional lithologies (Figure 1b; Padrón-Navarta, López-Sánchez-Vizcaíno, Garrido, & Gómez-Pugnaire, 2011). This contact shows no evidence of tectonic discontinuity (Trommsdorff et al., 1998) and represents the arrested dehydration front of Atg-serpentinite-producing Chl-harzburgite, that is, the Atg-out isograd according to the reaction:



Strongly foliated Atg-serpentinite (Atg+Ol+Mag±Di±Tr±Chl±Ti-Chu; all mineral abbreviations after Whitney & Evans, 2010) crops out in the upper portion of the massif (~200 m thick) and records several prograde dehydration reactions: brucite breakdown (López-Sánchez-Vizcaíno, Gómez-Pugnaire, Garrido, Padrón-Navarta, & Mellini, 2009; López-Sánchez-Vizcaíno et al., 2005), diopside transformation to tremolite (Jabaloy-Sánchez, Gómez-Pugnaire, Padrón-Navarta, López-Sánchez-Vizcaíno, & Garrido, 2015; Padrón-Navarta, Tommasi, Garrido, & López-Sánchez-Vizcaíno, 2012; Trommsdorff et al., 1998), titanian clinohumite breakdown (López-Sánchez-Vizcaíno et al., 2005, 2009), and antigorite reaction with talc to give orthopyroxene in SiO₂-rich serpentinites (Padrón-Navarta, Hermann, Garrido, López-Sánchez-Vizcaíno, & Gómez-Pugnaire, 2010). The Atg-serpentinite finally became

unstable at ~650°C and 16–19 kbar and dehydrated to prograde Chl-harzburgite (Ol+Opx+Chl+Mag±Tr±Ti-Chu), which reached a peak temperature of ~710°C at similar pressure (López-Sánchez-Vizcaíno et al., 2009; Padrón-Navarta, Tommasi, et al., 2010). Chl-harzburgite crops out in the lower part of the ultramafic body (~200 m thick) with either granofelsic or spinifex-like texture (see Padrón-Navarta Tommasi, et al., 2010; Padrón-Navarta et al., 2011).

Isotopic and trace element studies (Alt et al., 2012; Marchesi, Garrido, Padrón-Navarta, López-Sánchez-Vizcaíno, & Gómez-Pugnaire, 2013) show that the ultramafic protoliths of the Cerro del Almiraz serpentinites were transformed to chrysotile and lizardite serpentinites at ~200°C in a seafloor setting. The transformation of seafloor serpentinite into Atg-serpentinite during subduction most probably lowered the bulk ferric (Fe³⁺) to ferrous (Fe²⁺) iron ratio by magnetite dissolution into fluids (Debret et al., 2015). Further decrease in the amount of magnetite and bulk rock Fe³⁺/Fe_{Total} occurred by antigorite breakdown (Debret et al., 2015). The metarodingite bodies studied in this work occur in both Atg-serpentinite and Chl-harzburgite with granofelsic- or spinifex-like textures (Trommsdorff et al., 1998) and were first described by Puga, Nieto, Díaz de Federico, Bodinier, and Morten (1999). Similar metarodingite bodies have also been reported in the Cerro Blanco and Montenegro ultramafic outcrops in Eastern Sierra Nevada (Puga et al., 1999).

3 | METHODOLOGY

3.1 | Rock sampling

Twenty crosscuts of metarodingite and host ultramafic rocks were sampled from Cerro del Almiraz, seven in the Atg-serpentinite domain and 13 in the Chl-harzburgite domain (Figure 1b). Each crosscut includes a homogeneous sample of metarodingite, the metasomatic lithologies located between metarodingite and host ultramafic rocks, one sample of Atg-serpentinite or Chl-harzburgite in contact (<20 cm distant) with metarodingite, and one Atg-serpentinite or Chl-harzburgite located several metres distant from the metarodingite body.

3.2 | Bulk rock analyses

Rock chips were cut from homogeneous and unaltered parts of the samples, avoiding veins, contacts between different rock types and lithological zoning. Sample powders (mesh size ≤25 μm) were obtained by powdering representative crushates in an agate disc mill at the facilities of the Instituto Andaluz de Ciencias de la Tierra (IACT, CSIC-UGR, Granada, Spain).

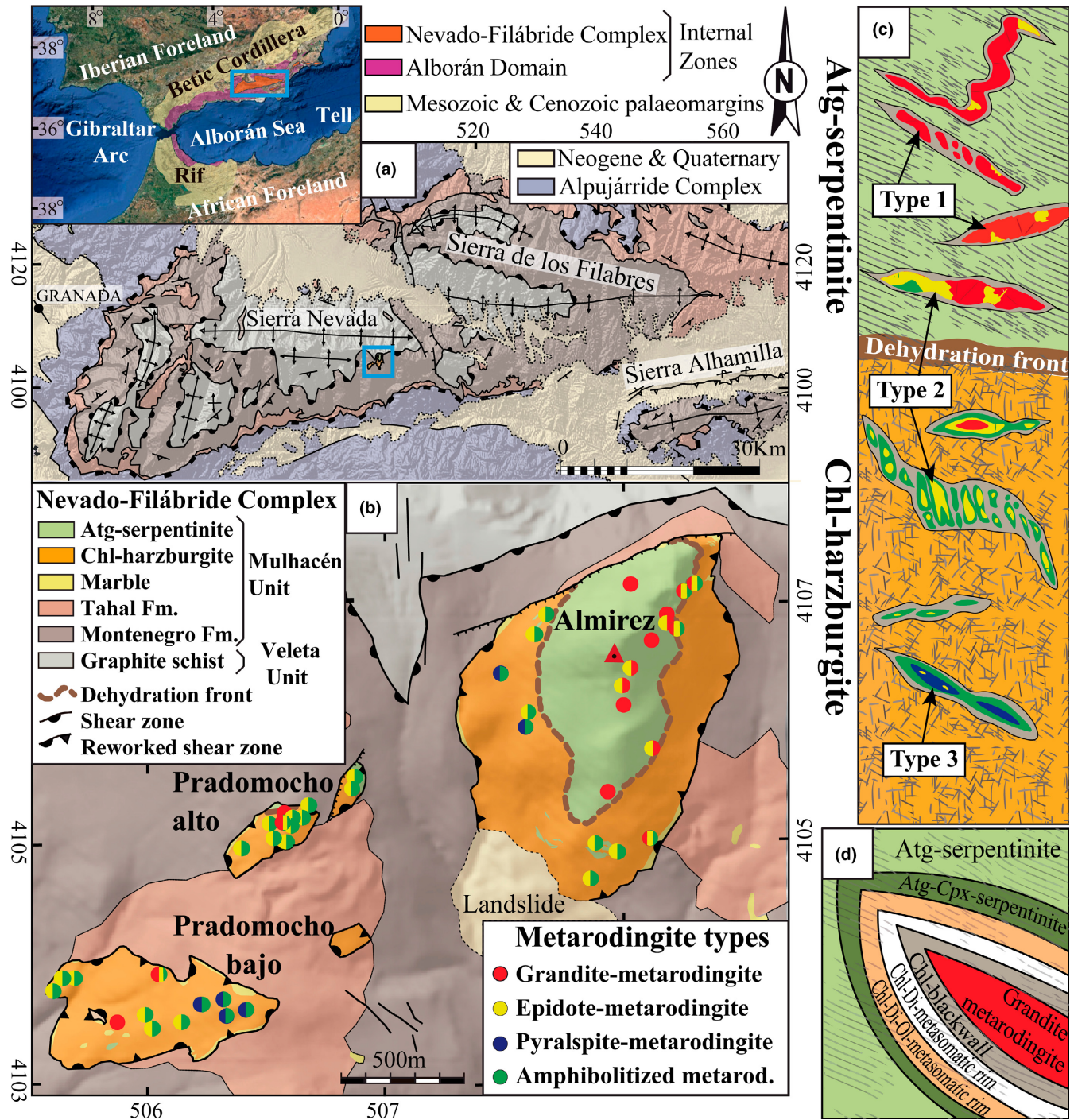


FIGURE 1 (a) Geological sketch map of the western part of the Nevado-Filábride Complex of the Betic Cordillera (modified from Jabaloy-Sánchez et al., 2015) with location of the Cerro del Almiraz ultramafic massif (blue inset) shown in (b). (b) Geological map of the Cerro del Almiraz area with the location of the sampled metaroddingite bodies. Coloured circles correspond to the reported metaroddingite types and amphibolitization degree. (c) Sketch column of the lithological sequence of the Cerro del Almiraz ultramafic massif showing the different types and shapes of metaroddingite bodies. Not to scale. Same colour key for metaroddingite types as in (b). The grey rim represents the metasomatic reaction rims altogether. (d) Sketch diagram with the distribution pattern of metasomatic reaction rims around a Grandite-metaroddingite boudin. Not to scale

Bulk-rock major and minor elements were analysed by X-ray fluorescence (XRF) in fused beads or pellets at IACT. Fused beads were made by weighing rock powders

(~1 g) with dilithium tetraborate flux and fusing the mixture at 1,000°C for 15 min. The analyses were performed using a BRUKER S4 Pioneer XRF instrument equipped

with six analysers (LiF200, LiF220, Ge, PE, PX1, PX2). Within-run precision (% relative *SD*), measured by repeated analyses of international reference materials as external standards, was better than 3% for all elements except Na and Mn (6%). Ferrous iron in bulk-rocks was determined by potentiometric titration with a standardized permanganate solution at the Geoscience Laboratories (GeoLabs) of the Ontario Geological Service (Canada).

3.3 | Electron microprobe analyses

Mineral analyses were obtained by a CAMECA SX100 electron microprobe at CIC (University of Granada, Spain) or a JEOL JXA-8230 electron microprobe at the Scientific and Technological Centres of UB (University of Barcelona, Spain). Both instruments operated with 15–20 kV acceleration voltage, 10–15 nA beam current, and 5 μm beam diameter. Precision was about $\pm 1.5\%$ for concentrations of 1 wt%. Natural minerals and synthetic glasses were used as standards. The peak measurement time was 10 s for Na, K, Mg, Ca, Al, Si, Mn, F and Cl, 20 s for Cr and Ti, and 30 s for Ni.

X-ray mapping was performed at 297 nA beam current and beam size spot (focused). The step (pixel) size was 2 μm and Dwell time 300 ms per pixel. X-ray maps were processed with the MATLAB[®]-based software XMapTools (Lanari et al., 2014).

3.4 | Scanning electron microscopy

Qualitative chemical maps were acquired on carbon coated thin sections using a Carl Zeiss scanning electron microscopy (SEM) equipped with Oxford/Nordlys EBSD and EDS detectors at the IACT. Automated mapping and data processing were done using the Aztec software from Oxford Instruments. Additional maps were acquired with a Leo 1430VP SEM at the CIC, equipped with an Inca 350 v. 17 Oxford Instruments EDS system.

4 | RESULTS

4.1 | Field occurrence and sample description

Metarodingites are heterogeneously distributed in the ultramafic domains of the Cerro del Almirez massif, that is, in Atg-serpentinite, Chl-harzburgite and close to the dehydration front defined by the Atg-out isograd (Figure 1b). The current location of metarodingite bodies is controlled by the original distribution of their protoliths and by their progressive deformation and disruption during subduction. Their metamorphic evolution resulted in a large variety of mineralogies, sizes, shapes, and mesostructures (Figure 1c; Table 1). According to them, three types of metarodingite

can be defined: Type 1 Grandite-metarodingite, Type 2 Epidote-metarodingite, and Type 3 Pyralspite-metarodingite.

Synmetamorphic interaction between metarodingites and host ultramafic rocks gave place to the progressive growth of chlorite-(Chl-) blackwalls and other metasomatic reaction rims (Figure 1d) of variable thickness (~7–40 cm).

4.1.1 | Structural features of metarodingite bodies

Metarodingites enclosed in Atg-serpentinite occur as boudinaged and disrupted layers up to 42 m in length and 1.8 m in thickness. They present different structures depending on the angle between the contact surface of the body and the main foliation of host serpentinite. Bodies subparallel or at low angles with the serpentinite foliation (Figure 2a,b) occur as boudin trains with different shapes depending on the intensity of shearing (Goscombe, Passchier, & Hand, 2004). Strike orientation of the boudins surfaces ranges from NE–SW to NW–SE and they dip between 20° and 45° mainly to N–NW and rarely to W–SW. Only one body, 15 m long and 0.75 m thick, has E–W strike and subvertical dip and is oblique to the serpentinite main foliation. In small shear zones in Atg-serpentinite (Jabaloy-Sánchez et al., 2015), asymmetric boudin trains of metarodingite are common (Figure 2c). In these cases, the rodingite boudins are disrupted by small shear zones and rotated, forming decimetric ellipsoidal bodies embedded in Chl-blackwalls (Figure 2c). Chl-blackwalls have a well-developed schistosity continuous with the penetrative S_1 foliation of Atg-serpentinite (Figure 2a,b; Jabaloy-Sánchez et al., 2015).

In the Atg-serpentinite-hosted metarodingites, two sets of conjugate fractures are found with low (<60°) dihedral angles and are few millimetres to two centimetres thickness, filled with garnet, chlorite or epidote (Figure 2a,d).

Metarodingites enclosed in Chl-harzburgite mostly occur as small isolated boudins usually <1 m in length and 50 cm thick (Figure 2e,f). Rare decametric boudin trains, some of them folded, are also visible. The contact surface orientation of these metarodingite bodies is variable and ranges between NE and SW strike with 30–50° dip to NW or SE, and E–W strike with dip to the south ranging between 50° and subvertical. Millimetre thick conjugate hybrid joints are commonly filled by amphibole in these metarodingites (Figure 2d,e). Chl-blackwalls show a well-developed S_2 schistosity with transposed hinges of the S_1 foliation of Atg-serpentinite (Figure 3a). In some outcrops, especially in the Pradomocho Alto and Pradomocho Bajo ultramafic bodies (Figure 1b), alternating layers of Chl-blackwall and amphibolitized metarodingite define a well-marked banding parallel to S_2 (Figure 2f). In places, a late

TABLE 1 Summary of the Cerro del Almirez metaroddingite types and associated metasomatic reaction rims

Host rock	Lithologies	Key macroscopic and textural features	Minerals and modal percentage (vol.%)	Mineral assemblages in equilibrium
Atg-Serp	Grandite-metaroddingite Type 1	Reddish brown, fine-grained rocks with relict igneous texture (porphyritic). With several veins generations	(Grt-1+Grt-2+Grt-3) 66%+Chl 23%+Di 6.5%+Ttn 3%+Mag 2.7%+Ap 1%+Ilm+Aln+Zrn	Grt-1+Chl+Di+Mag+Ilm Grt-2a+Chl+Di+Mag+Ilm Grt-2b+Chl+Ttn±Di Grt-3+Chl+Ttn
Atg-Serp & Chl-Harzb	Epidote-metaroddingite Type 2	Yellowish, fine-grained rocks with granoblastic texture and relict garnet	Ep 55%+Di 35%+Ttn 5%+(Grt-3 or Grt-4) 3.5%±Chl+Ap 1%±Mag±Rt+Ilm+Zrn	Ep+Di+Ttn±Grt-3±Chl Ep+Di+Ttn±Grt-4±Chl
Chl-Harzb	Pyralpsite-metaroddingite Type 3	Blackish green and greenish yellow rocks with granoblastic or nematoblastic texture	Amp 50%+Ep/Zo 35%+Grt-5 10%±Chl 0-4%±Di 1%+Rt 2%+Ap 1%±Ttn±Ilm+Zrn	Grt-5+Ep/Zo+Amp-1±Chl±Di+Ttn Grt-5+Ep/Zo+Amp-1±Chl+Rt
Atg-Serp & Chl-Harzb	Chl-Blackwall	Silverish grey, strongly foliated rock	Chl 70%+Di 22%±Ttn 2%±Mag 2.7%±Ilm 2.7-4%±Rt 0-2%+Ap 0.6%±Amp+Zrn	Ch+Di+Ttn+Mag Chl+Di+Ilm Chl+Amp-1+Rt
Atg-Serp & Chl-Harzb	Chl-Di-metasomatic rim	Bluish white, foliated rock	Di 60%+Chl 35%+Mag 4%+Ilm	Di+Chl+Mag+Ilm
Atg-Serp & Chl-Harzb	Chl-Di-Ol-metasomatic rim	Foliated rock with orangish brown Ol porphyroblasts, and Ti-Chu	Di 36%+Ol 36%+Chl 21%+Mag 5%±Ti-Chu±Atg	Ol+Di+Chl+Mag+Ti-Chu

crenulation cleavage (S_3) affects the S_2 foliation (Figures 2f and 3a). In contrast with the nondeformed Chl-harzburgite host (Jabaloy-Sánchez et al., 2015; Padrón-Navarta, Tommasi, et al., 2010), S-C structures in diopside-rich reaction rims (Figure 3b) indicate a top-to-the-west sense of shearing, similar to those of Atg-serpentinite and hosting metapelites (Jabaloy-Sánchez et al., 2015).

4.1.2 | Metaroddingite types and petrography

Metaroddingites have different mineralogical and microstructural features at each side of the dehydration front (Figure 1b,c). No systematic differences exist between metaroddingite bodies hosted in Chl-harzburgite with spinifex-like or granofelsic texture.

Type 1 Grandite-metaroddingite (in the following Grand-metaroddingite) consists of Grs- and/or Adr-rich Grt+Chl+Di+Ttn+Mag+Ap+Ilm+Aln+Zrn (Table 1). This is the most abundant type of metaroddingite enclosed in Atg-serpentinite (Figures 1b,c and 2a–d). In Chl-harzburgite, it is preserved only as small relicts in the core of some Type 2 metaroddingite boudins.

Macroscopically, Grand-metaroddingite shows a reddish, garnet-rich groundmass. Porphyritic igneous textures typical of basaltic rocks are preserved in places (Figure 4a). At the thin section scale, Grand-metaroddingite shows a very fine-grained (5–50 μm) matrix consisting of allotriomorphic aggregates of anhedral pinkish or brownish garnet (Grt-1

hereafter), chlorite, titanite and less abundant diopside (Figure 4a,b). The fine-grained Grt-1 aggregates replaced plagioclase in the original igneous doleritic or fluidal textures as well as plagioclase phenocrysts (1–3 cm) in porphyritic basalts (Figure 4a,c). Pseudomorphs after igneous clinopyroxene are replaced by diopside with tiny magnetite, ilmenite, and titanite exsolutions or, more rarely, by garnet-diopside symplectites. Rare olivine phenocrysts were transformed into dark pseudomorphs of chlorite–diopside–titanite–magnetite (0.5–2 cm). In the most deformed samples, igneous textures partially or completely recrystallized to homogeneous granoblastic or slightly oriented textures. The modal abundance of chlorite increases towards the contact with the Chl-blackwall.

Garnet veins of variable thickness (up to 2 cm) frequently cut the rock matrix (Figure 2a,d). Two vein generations can be distinguished (Figure 4b). The older veins are thin (<1 cm), display irregular rims, and mainly consist of Grt-2 garnet (see Section 4.2.1; Figure 4b). Grt-2 has a small grain size (<50 μm) and occurs in massive aggregates with titanite and minor chlorite. The second vein generation mostly consists of Grt-3 garnet (see Section 4.2.1). These veins always cut those containing Grt-2 (Figure 4b). They are decimetric in length and up to 2 cm thick (Figure 2d). Grt-3 occurs as drusy, projecting aggregates of coarse (1–2 mm) idiomorphic grains, usually intergrown with chlorite flakes, rare diopside or epidote, apatite and large titanite crystals (up to 6 cm; inset in Figure 2d). Both

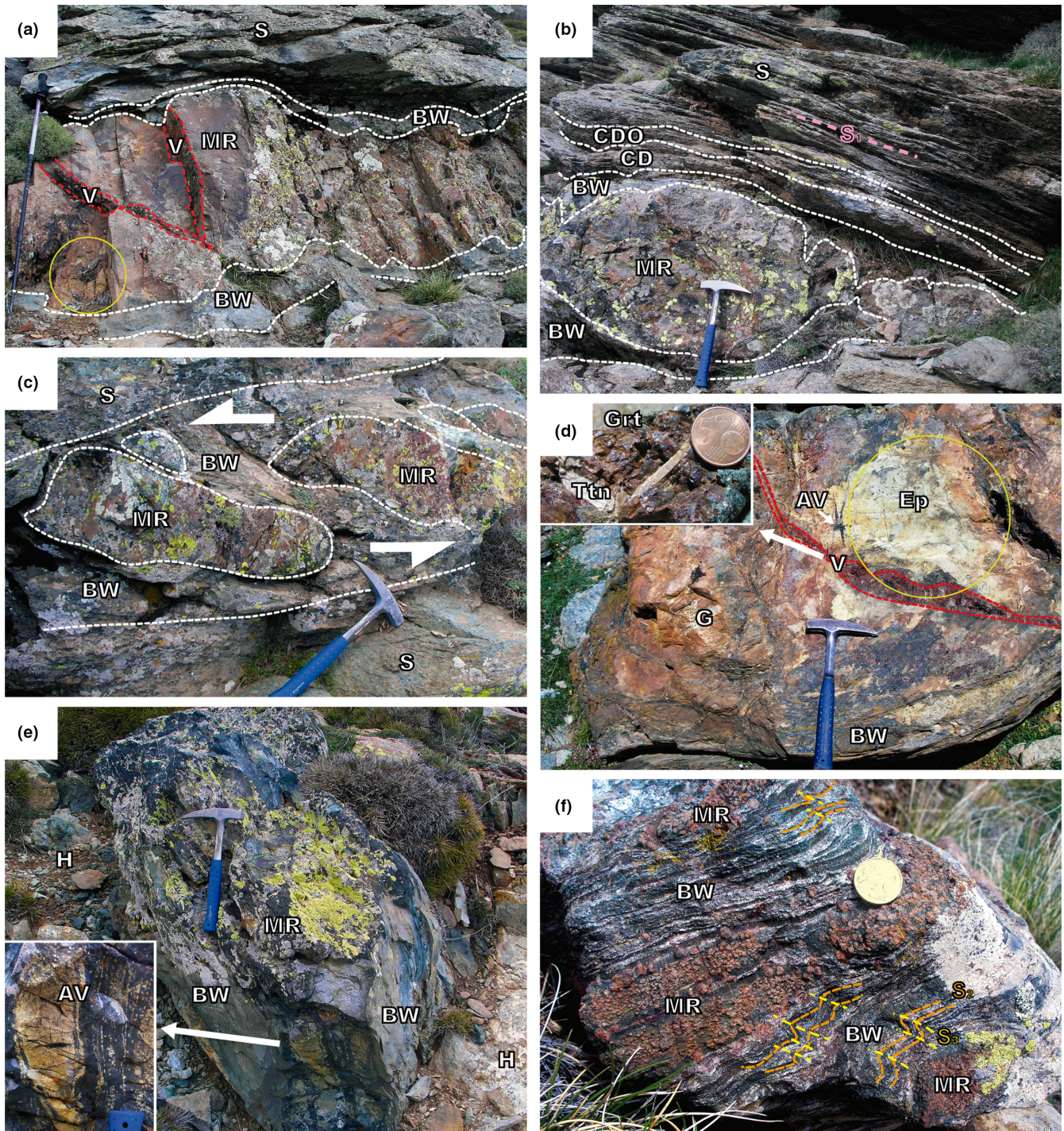


FIGURE 2 Field occurrence of metaroddingite bodies in the Cerro del Almirez ultramafic massif. (a) Type 1, Grand-metaroddingite dyke hosted in Atg-serpentinite with incipient transformation into Epidote-metaroddingite (yellow circle). (b) Barrel-shaped boudin of Grand-metaroddingite hosted in Atg-serpentinite with well-developed S_1 foliation and metasomatic rims. (c) Asymmetric boundin trains of Grand-metaroddingite hosted in Atg-serpentinite separated by small shear fractures in the Chl-blackwall. The sense of shear is indicated. (d) Atg-serpentinite-hosted, zoned boudin with well-defined Grand- (to the left; G) and Ep-metaroddingite (to the right; Ep) zones cut by a thick Grt-3 vein (enlarged in the upper left inset showing coarse garnet and titanite crystals). Note also two amphibole veins (AV). (e) Partially amphibolitized Type-2, Ep-metaroddingite boudin enclosed in Chl-harzburgites (H). Enlarged inset: epidote-rich core cut by amphibole veins (AV). (f) Partially amphibolitized, Type-3, Pyrralspite-metaroddingite boudin with folded S_2 foliation in Chlorite-blackwall and late development of S_3 crenulation cleavage. MR: metaroddingite; V: garnet veins; S: Atg-serpentinite; BW: Chlorite-blackwall; (CD) Chlorite-diopside metasomatic rim, (CDO) Chlorite-diopside-olivine-metasomatic rim

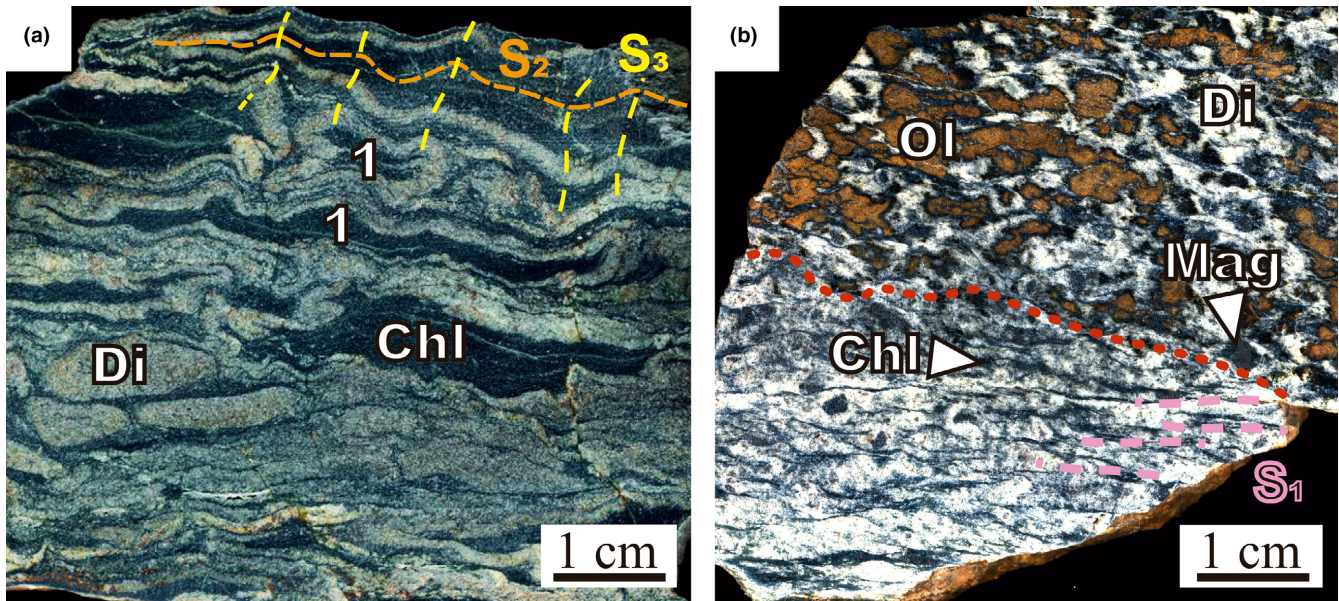


FIGURE 3 (a) Polished surface of a Chl-blackwall hand sample with alternating layers of chlorite (Chl) and diopside (Di). It corresponds to an Ep-metarodinite hosted in Chl-harzburgite. Note the sheath folds (1) parallel to S_2 foliation, typical of shear zones and late S_3 crenulation cleavage. (b) Polished surface of a hand-sample with the chlorite–diopside- (lower part) and chlorite–diopside–olivine- (upper part) metasomatic rims of a Grand-metarodinite hosted in Atg-serpentinite

Grt-2 and Grt-3 may also occur in the rock matrix rimming Grt-1. These three garnet generations display slight anisotropy produced either by cell distortion due to the occurrence of OH groups (Andrut, Wildner, & Beran, 2002) or to strain caused by the intergrowth of different cubic phases (e.g., Antao, Zaman, Gontijo, Camargo, & Marr, 2015). Exploratory infrared measurements confirm the occurrence of OH-groups in the Grand-metarodinite garnets as well as in diopside (Figure S1).

The occurrence of epidote in Type 1 metarodinite marks the transition to Type 2 Epidote-metarodinite (in the following Ep-metarodinite). This consists of $Ep+Di\pm Grt\pm Chl\pm Ttn+Ap+Zrn\pm Mag\pm Rt\pm Ilm$ (Table 1). Evidence of incipient transformation from Type 1 to Type 2 metarodinites is visible in almost each Grand-metarodinite outcrop (Figure 2a). However, in the Atg-serpentinite domain, well-developed Ep-metarodinite assemblages are present only in some zoned boudins close to the dehydration front (Figure 1c), in which they show irregular or patchy, sharp contacts with the garnet-rich zones (Figure 2d). Type 2 is the most common metarodinite type within dehydrated Chl-harzburgite, where it is usually observed in the core of boudins that are partially transformed by late, retrograde amphibolitization (see below; Figures 2e and 4c).

The Ep-metarodinite is a fine-grained, granoblastic, yellowish rock. The matrix is made of polygonal (5–200 μm) epidote and diopside aggregates, formed after garnet, with disseminated chlorite flakes that are less abundant towards the core of the bodies. Porphyroblasts consisting

of fine-grained Grt-1 aggregates are here replaced by coarse epidote grains (Figure 4c). Small metastable relicts of Grt-2 and Grt-3 are also visible (Figure 4c,d). However, in some Atg-serpentinite-hosted bodies, some of these garnet grains (with a Grt-3 composition) are in equilibrium with the epidote–diopside–titanite assemblage. In a similar way, scarce grains of a different garnet (Grt-4, See Section 4.2.1) are present in the Ep-metarodinite bodies hosted in Chl-harzburgite. The Grt-4 occurs as small xenomorphic grains locally overgrown by idioblastic recrystallized rims (Figure 4e). Titanite is more abundant than in Type 1 metarodinite (Table 1) and forms aggregates (2–6 mm) disseminated in the matrix (which may include rutile) or thin (0.5 mm) irregular veins.

Type 3 Pyralspite-metarodinite (in the following Pyral-metarodinite) crops out only in the Chl-harzburgite domain (Figure 1b,c). In the field, it constitutes compact, decimetre long, ellipsoidal bodies embedded in a banded blackwall consisting of chlorite-rich light and amphibole-rich dark layers (Figure 2f). The typical metarodinite assemblage consists of neoblasts of a new pyralspitic garnet generation Grt (Grt-5, see Section 4.2.1) $+Ep+Zo+Amp$ ($Amp-1\pm Chl\pm Di+Rt+Ap+Zrn\pm Mag\pm Ttn\pm Ilm$) (Table 1). Grt-5 occurs as porphyroblasts of variable abundance and grain size. It is more abundant and smaller (1–3 mm) in the massive cores of the boudins, where they are rich in inclusions of colourless or slightly pleochroic amphibole (Amp-1), chlorite, epidote, zoisite, apatite, rare diopside, titanite in the core, and rutile in the rim (Figure 4f). Grt-5 porphyroblasts are hosted in a grano to nematoblastic matrix mainly

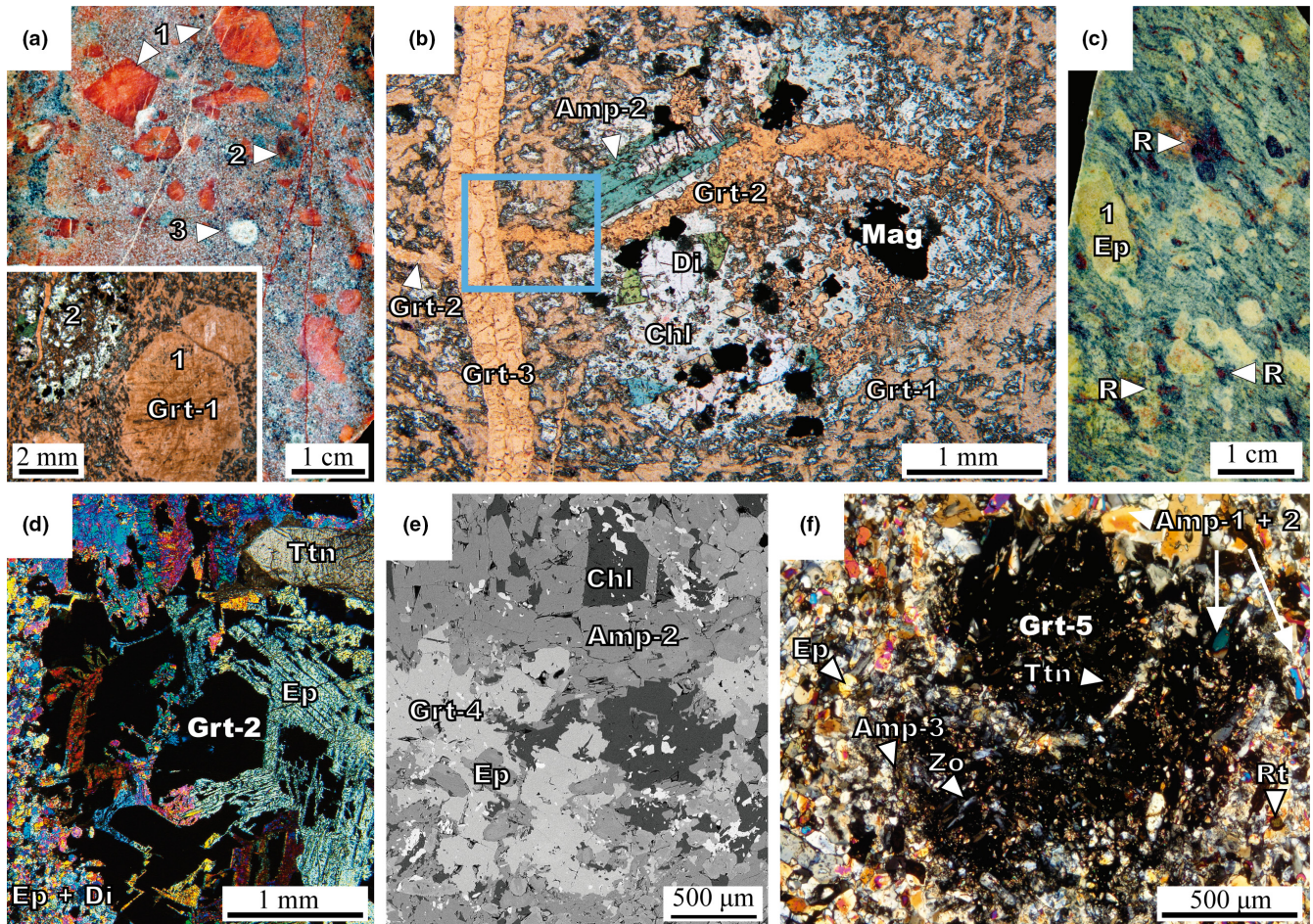


FIGURE 4 (a) Polished surface of a Grand-metaroddingite hand-sample with preserved porphyritic igneous texture. Lower left inset: same texture at thin section scale (parallel polars). (1) Garnet (Grt-1) pseudomorph after igneous plagioclase. (2) Igneous olivine replaced by chlorite, magnetite and diopside. (3) Igneous Ti-augite replaced by diopside, magnetite and ilmenite. (b) Texture of Grand-metaroddingite at thin section with two vein generations mainly consisting of Grt-2 and Grt-3 respectively. Diopside was partially replaced by late green amphibole (Amp-2; parallel polars). The blue inset corresponds to the compositional maps area in Figure 6a,b. (c) Polished surface of an amphibolitized Ep-metaroddingite hand-sample with preserved porphyritic igneous textures (1) and garnet relicts (R). (d) Ep-metaroddingite at thin section with garnet relicts (Grt-2b) of a vein partially transformed into epidote (crossed polars). (e) SEM image of Ep-metaroddingite hosted in Chl-harzburgite with recrystallized garnet relicts reequilibrated to Grt-4. (f) Pyrral-metaroddingite at thin section with a Grt-5 porphyroblast crowded with titanite inclusions in the core and zoisite (Zo) and amphibole inclusions (Amp-1) in the rims. Matrix with amphibole (Amp-1 and Amp-2), epidote, zoisite and rutile (Rt). Amp-3 altered garnet rims. Crossed polars

consisting of epidote and zoned green-pleochroic amphibole (Amp-2) with colourless cores of Amp-1, chlorite, zoisite, rare diopside, and rutile and apatite as accessory phases.

Towards the Chl-blackwall, the modal abundances of epidote and diopside decrease until their complete disappearance, chlorite and zoned amphibole define a well-marked foliation (S_2), and Grt-5 porphyroblasts are less abundant but coarser (up to 6 mm). The rims of these garnet porphyroblasts are commonly corroded by late fine-grained chlorite. Amphibole, titanite and rutile inclusions in garnet are here arranged in rotated trails defining snowball orientations that are continuous with the matrix foliation. This rotation was due to the shearing responsible for the

formation of banding and S_2 foliation (Jabaloy-Sánchez et al., 2015). This event was previous to the growth of the green pleochroic rims of amphibole (Amp-2). Late crenulation (Figures 2f and 3a) defines a S_3 foliation and postdates the main metamorphic assemblage.

4.1.3 | Amphibolitization of metaroddingites

The growth of late amphibole (Amp-2) replacing previous mineral assemblages is common in all the metaroddingite types. The intensity of amphibolitization is, however, very variable. In Grand-metaroddingite within Atg-serpentinite, Amp-2 constitutes late, green, idiomorphic grains that

overgrow diopside and corrode garnet (Figure 4b). In boudins close to the dehydration front, centimetre thick, irregular bands or aggregates of dark amphibole are common. Conjugated sets of millimetre-thick amphibole veins are also very abundant (Figure 2d) as well as reopened coarse-grained garnet (Grt-3) veins (Figure 2d) refilled with aggregates of centimetre long, prismatic amphibole.

Within Chl-harzburgite, all Ep-metarodingite boudins are partially replaced by dark green aggregates of Amp-2 (Figure 2e). Typically, the preserved epidote-rich cores are crosscut by conjugated sets of millimetre-thick amphibole veins (Figure 2e).

In Pyrrals-metarodingite and enclosing Chl-blackwall, amphibolitization can be also related with the growth of Amp-2. Grt-5 porphyroblasts are strongly corroded by a later, fine-grained amphibole corona (Amp-3; Figure 4f).

4.1.4 | Metasomatic reaction rims

Interaction between metarodingites and host Atg-serpentinite produced three metasomatic rock types that are, from the metarodingite body to the enclosing serpentinite, the following chlorite- (Chl-) blackwall, chlorite-diopside- (Chl-Di-) rim and chlorite-diopside-olivine- (Chl-Di-Ol-) rim (Figure 1d). In the Chl-harzburgite domain, only the first two lithologies are generally well developed.

The Chl-blackwall (5–20 cm thick) is a light silver, strongly foliated, Chl-Di schist (Figure 2) with $\pm\text{Ttn}\pm\text{Ilm}\pm\text{Rt}\pm\text{Mag}+\text{Ap}+\text{Zrn}$. This rock essentially consists of alternating chlorite- and diopside-rich layers and veins parallel to the main foliation (Figure 3a). Due to intense deformation, blackwalls in the Chl-harzburgite domain may constitute strongly thinned bands transposed from metarodingites. The contact between the Chl-blackwall and metarodingite is generally sharp (Figure 2a,b). In some places, rare epidote, amphibole or garnet-isolated grains or veins are visible within the blackwall.

At the thin section scale, Chl-blackwall has a clearly lepidoblastic texture marked by the preferred orientation of chlorite flakes. Diopside constitutes hypidiomorphic-isolated grains or granoblastic aggregates. In the Atg-serpentinite domain, oriented titanite (up to 1.5 cm) and magnetite grains are abundant, while ilmenite is less common. The Chl-blackwalls in the Chl-harzburgite domain lack magnetite but have large (up to 1 cm) idiomorphic pyrite crystals, abundant ilmenite and, around Pyrrals-metarodingite, they also have rutile. Rare titanite appears only close to Ep-metarodingite bodies.

The Chl-Di- and Chl-Di-Ol-metasomatic rims have variable thicknesses (2–20 cm). The former is a whitish rock with nematoblastic texture, thin dark intercalations of chlorite between diopside and disseminated magnetite grains. The contact with the Chl-Di-Ol-rim is defined by the first

occurrence of millimetre to centimetre long brownish aggregates of olivine, which confer a “leopard skin” appearance on the rock (Figure 3b). Olivine aggregates have dark iddingsitic alteration rims and are in places intergrown with titanite-clinohumite. These aggregates are embedded in a granoblastic matrix of dusty diopside with clear rims. Chlorite flakes commonly have antigorite relicts in the core. Magnetite is disseminated in the rock. The contact with Atg-serpentinite is transitional and defined by the increasing amount of antigorite, the decrease of diopside and the absence of chlorite (Antigorite-Clinopyroxene serpentinite, Figure 1d).

4.2 | Mineral chemistry

4.2.1 | Garnet

According to their composition, the different types of garnet can be classified into two main groups: grandite- (Grt-1, Grt-2, and Grt-3) and pyrralspite-garnet (Grt-5), with a third group (Grt-4) of intermediate composition (Table 2 and Table S1).

Grandite-garnet corresponds to the main rock-forming mineral of Grand-metarodingite and to relict grains in Ep-metarodingite hosted by Atg-serpentinite. These compositions plot along the Grossular-Andradite side in Figure 5 and their pyrralspite components (pyrope, almandine and spessartine end-members altogether) are below 25 mol.%. Several types of grandite garnet can be defined taking into account their textural and compositional features (Table 2; Figure 5). Grt-1 has the highest grossular values and lowest andradite and pyrralspite contents (Grs_{64-84} Adr_{5-19} Prp_{0-1} Alm_{0-3} Sps_{0-1} Ti-Grt_{2-11} Kat_{1-5}).

Two subtypes of Grt-2 have been differentiated. Grt-2a only occurs as very scarce grains within the first vein generation in Grand-metarodingite (Figure 6a,b). It has a peculiar pyrralspite-poor composition (Grs_{55-59} Adr_{20-24} $\text{Prp}_{0.7-0.9}$ $\text{Alm}_{0.7-0.9}$ $\text{Sps}_{0.2-0.6}$ Ti-Grt_{13-16} $\text{Kat}_{1.9-3.4}$) when compared with the most abundant garnet type in these veins: Grt-2b (Grs_{42-61} Adr_{21-31} Prp_{3-7} Alm_{7-13} $\text{Sps}_{0.6-1}$ Ti-Grt_{3-9} Kat_{2-3}), richer in andradite and pyrralspite end-members than Grt-1 (Figure 5). Grt-2b overgrows the Grt-2a grains in the first vein generation (Figure 6a,b). The Grt-2b relicts are found in Ep-metarodingite boudins from both the Atg-serpentinite and the Chl-harzburgite domains (blue triangles and blue squares in Figure 5, respectively).

Grt-3 is poorer in pyrralspite and richer in andradite than Grt-2b (Grs_{38-56} Adr_{31-45} Prp_{1-4} Alm_{3-8} $\text{Sps}_{0.4-0.8}$ Ti-Grt_{5-10} Kat_{2-4}), especially the grains in Ep-metarodingites (Grs_{34-38} Adr_{49-53} Prp_{1-3} Alm_2 Sps_2 Ti-Grt_{4-5} Kat_{2-3} , dark yellow triangles in Figure 5). Grt-3 grains from the second vein generation in Grand-metarodingite (Figure 4b) display a drusy texture and oscillatory zoning in their

TABLE 2 Garnet average compositions and *SD* (σ) of microprobe analyses

Garnet																
Garnet type	Grt-1		Grt-2a		Grt-2b		Grt-3			Grt-4		Grt-5 core		Grt-5 rim		
	Type 1		Type 1		Type 1		Type 1	Type 2		Type 2		Type 3		Type 3		
Metarod. type																
<i>n</i>	33		11		72		84	7		14		19		29		
SiO ₂	37.11	0.21	36.65	0.19	37.49	0.53	36.53	0.28	36.45	0.10	38.53	0.31	37.69	0.36	38.89	0.43
TiO ₂	1.94	0.12	2.52	0.22	0.78	0.21	1.23	0.28	0.79	0.07	0.32	0.28	0.17	0.13	0.09	0.04
Al ₂ O ₃	16.91	0.44	13.36	0.22	14.77	0.93	12.05	0.78	9.42	0.34	19.93	1.33	21.02	0.17	21.56	0.30
Cr ₂ O ₃	0.01	0.01	0.02	0.01	0.07	0.18	0.03	0.10	0.10	0.03	0.07	0.02	0.00	0.01	0.01	0.02
FeO tot.	5.68	0.74	9.77	0.35	13.46	0.72	14.34	0.76	16.63	0.33	13.63	1.57	23.63	0.30	18.99	0.85
MnO	0.26	0.02	0.20	0.05	0.48	0.10	0.28	0.06	0.89	0.09	2.50	1.07	1.17	0.07	0.54	0.29
MgO	0.13	0.04	0.18	0.03	1.23	0.20	0.70	0.14	0.35	0.15	3.70	1.97	3.26	0.32	7.04	0.37
CaO	35.60	0.36	34.01	0.45	29.96	0.73	32.12	0.55	32.95	0.12	20.65	4.66	12.53	0.37	12.55	0.89
Na ₂ O	0.00	0.00	0.01	0.00	0.01	0.01	0.01	0.01	0.02	0.01	0.01	0.02	0.00	0.00	0.00	0.00
H ₂ O ⁺	1.03	0.15	0.59	0.11	0.43	0.25	0.71	0.17	0.55	0.11	0.05	0.09	0.00	0.00	0.00	0.00
Total	98.69	0.27	97.31	0.85	98.67	0.54	98.00	0.43	98.15	0.31	99.38	0.57	99.49	0.50	99.68	0.55
Final FeO	2.06	0.27	3.12	0.30	5.29	0.59	3.49	0.43	1.58	0.11	10.82	1.98	22.16	0.41	17.41	0.68
Final Fe ₂ O ₃	4.02	0.79	7.39	0.41	9.08	1.02	12.06	0.87	16.72	0.40	3.12	1.42	1.63	0.46	1.76	0.76
Total	99.09	0.29	98.05	0.86	99.58	0.53	99.21	0.44	99.83	0.30	99.69	0.54	99.65	0.46	99.86	0.50
<i>Structural formula is calculated on the basis of 12 oxygen atoms and end-member fraction after Locock (2008)</i>																
Si	2.87	0.02	2.92	0.01	2.94	0.03	2.91	0.02	2.93	0.01	2.98	0.01	2.97	0.01	2.97	0.02
Al	0.00	0.00	0.00	0.00	0.00	0.00	0.00	0.00	0.00	0.00	0.02	0.02	0.03	0.01	0.03	0.02
4H ⁺	0.13	0.02	0.08	0.01	0.06	0.03	0.09	0.02	0.07	0.01	0.01	0.01	0.00	0.00	0.00	0.00
Ti	0.11	0.01	0.15	0.01	0.05	0.01	0.07	0.02	0.05	0.00	0.02	0.02	0.01	0.01	0.01	0.00
Al	1.54	0.04	1.25	0.03	1.37	0.08	1.13	0.07	0.89	0.03	1.80	0.11	1.92	0.02	1.91	0.03
Cr	0.00	0.00	0.00	0.00	0.00	0.01	0.00	0.01	0.01	0.00	0.00	0.00	0.00	0.00	0.00	0.00
Fe ²⁺	0.11	0.01	0.15	0.01	0.05	0.01	0.07	0.02	0.04	0.00	0.01	0.02	0.00	0.00	0.00	0.00
Fe ³⁺	0.23	0.05	0.44	0.02	0.54	0.06	0.72	0.05	1.01	0.03	0.18	0.08	0.10	0.03	0.10	0.04
Fe ²⁺	0.02	0.02	0.06	0.02	0.30	0.05	0.16	0.03	0.06	0.01	0.69	0.14	1.46	0.02	1.11	0.04
Mn ²⁺	0.02	0.00	0.01	0.00	0.03	0.01	0.02	0.00	0.06	0.01	0.16	0.07	0.08	0.00	0.04	0.02
Mg	0.01	0.01	0.02	0.00	0.14	0.02	0.08	0.02	0.04	0.02	0.43	0.23	0.38	0.04	0.80	0.04
Ca	2.95	0.02	2.90	0.02	2.52	0.07	2.74	0.05	2.83	0.01	1.71	0.39	1.06	0.03	1.03	0.07
<i>End-members (mol.%)</i>																
Grossular	70.79	2.31	57.01	1.46	50.56	3.06	44.65	2.84	36.65	1.56	47.05	9.83	31.86	0.91	30.74	2.89
Andradite	11.69	2.32	22.16	1.20	26.85	3.08	36.09	2.71	50.50	1.31	8.02	4.54	2.84	0.45	3.20	1.01
Almandine	0.72	0.61	1.95	0.51	10.07	1.55	5.32	1.09	2.04	0.22	22.89	4.59	48.61	0.75	37.09	1.45
Pyrope	0.45	0.21	0.73	0.11	4.79	0.77	2.75	0.56	1.38	0.60	14.20	7.53	12.76	1.20	26.74	1.42
Spessartine	0.57	0.05	0.46	0.11	1.07	0.23	0.64	0.13	2.02	0.20	5.45	2.36	2.60	0.17	1.18	0.64
Katoite	4.44	0.64	2.60	0.47	1.86	1.09	3.12	0.74	2.47	0.46	0.23	0.38	0.00	0.00	0.00	0.00
Morimotoite	11.14	0.58	14.98	1.25	4.52	1.25	7.28	1.66	4.47	0.46	1.17	1.85	0.01	0.05	0.01	0.04
Uvarovite	0.04	0.03	0.05	0.02	0.23	0.57	0.10	0.33	0.32	0.09	0.21	0.07	0.01	0.03	0.04	0.08
Hutcheonite	0.00	0.00	0.01	0.02	0.00	0.00	0.00	0.00	0.00	0.00	0.30	0.36	0.49	0.35	0.26	0.11
NaTi garnet	0.03	0.03	0.05	0.02	0.06	0.07	0.04	0.05	0.14	0.05	0.04	0.07	0.00	0.00	0.00	0.00
Morimotoite-Mg	0.10	0.25	0.00	0.00	0.00	0.00	0.00	0.00	0.00	0.00	0.00	0.00	0.00	0.00	0.00	0.00

H₂O⁺ values are estimated to be equal to the amount compensating for the deficiency of silica.

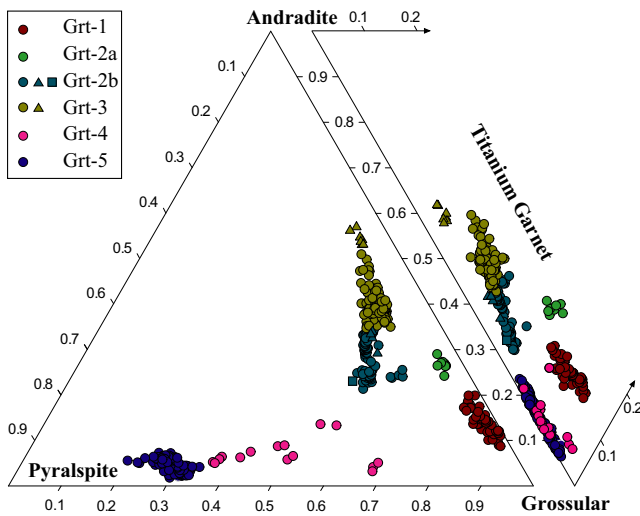


FIGURE 5 Ternary plots with the composition of the different garnet generations found in the Almirez metarodingites. Pyralpsite sums up the amounts of pyrope, almandine and spessartine components. Titanium garnet mainly corresponds to morimotoite component. Triangle symbols correspond to relicts of granditic garnet (Grt-2b and Grt-3) in Ep-metarodingite hosted in Atg-serpentinite. Squares represent relicts of granditic (Grt-2b) garnet in the cores of the Grt-4 grains in Ep-metarodingites hosted in Chl-harzburgites

andradite content (35–45 mol.%, Figure 6a). This is typical of hydrothermal andraditic garnet precipitating in voids and cracks full of fluid (Jamtveit & Andersen, 1992). In these veins, Grt-3 is crosscut by irregular thin veinlets with Grt-2b composition (stars in Figure 6a,b). Thin rims of Grt-3 also surround both Grt-1 and Grt-2 in Grand-metarodingite (Figure 6a,b).

All the grandite-garnet is rich in OH (katoite end-member: $\text{Ca}_3\text{Al}_2\text{OH}_{12}$; Table 2), especially Grt-1 (up to 5 mol.%), and in the Ti-bearing morimotoite end-member ($\text{Ca}_3[\text{TiFe}^{2+}]\text{Si}_3\text{O}_{12}$). The latter component is abundant in Grt-1 (up to 11 mol.%) and especially in Grt-2a (up to 16 mol.%) and poorer in Grt-2b (3–9 mol.%) and Grt-3 (5–10 mol.%). Schorlomite ($\text{Ca}_3\text{Ti}_2[\text{Fe}_2^{3+}\text{Si}]\text{O}_{12}$) and NaTi-garnet ($[\text{Na}_2\text{Ca}]\text{Ti}_2\text{Si}_3\text{O}_{12}$) end-members only occur in scarce amounts.

The pyralpsite-garnet (Grt-5) only occurs in Type 3 Pyralps-metarodingite. It has more than 60 mol.% of pyralpsite components: Grs_{17-35} Adr_{2-7} Prp_{10-30} Alm_{35-50} Sps_{1-10} (Table 2, Figure 5). Grt-5 shows pyrope enrichment and almandine and spessartine depletion from the core (Grs_{28-35} Adr_{1-2} Prp_{10-17} Alm_{47-50} Sps_{2-4}) to the rims (Grs_{28-31} Adr_{1-2-3} Prp_{22-28} Alm_{35-41} Sps_{0-1} ; Figure 6c). Towards the Chl-blackwall, the grossular component in Grt-5 is lower, but it increases from the core (Grs_{17} Adr_{4-7} Prp_{17} Alm_{45} Sps_{10}) to the rims (Grs_{27} Adr_{4-7} Prp_{30} Alm_{35} Sps_4).

Finally, Grt-4 grains in Ep-metarodingite (Table 2 and Table S1; Figure 4e) have intermediate compositions between those of grandite- and pyralpsite-garnet groups (Grs_{35-52} Adr_{5-20} Prp_{6-23} Alm_{13-30} Sps_{3-10} Ti-Grt_{0-6} Kat_{0-2} ; pink circles in Figure 5). Individual Grt-4 grains display a well-defined core to rim increase of the pyralpsitic components.

4.2.2 | Chlorite

Chlorite has different compositional ranges in different rock types (Table S1). In metarodingites, irrespective of the rock type and textural position, this phase has sheridanite-clinocllore compositions ($X_{\text{Mg}} = \text{Mg}/(\text{Mg} + \text{Fe}^{2+}) = 0.86\text{--}0.90$, $\text{Al}/\text{Si} = 0.80\text{--}0.90$). Chlorite in Chl-blackwall has slightly higher X_{Mg} (0.89–0.95) and lower Al/Si (0.60–0.79) corresponding to the clinocllore and penninite end-members. In the Chl-Di- and Chl-Di-Ol- metasomatic rims, chlorite has similar and rather constant Mg-rich, Al-poor compositions ($X_{\text{Mg}} = 0.93\text{--}0.96$; $\text{Al}/\text{Si} = 0.44\text{--}0.57$), mostly corresponding to penninite. However, in the Chl-Di-Ol-rim, it has high Cr_2O_3 contents (up to 2 wt%) that are negatively correlated with Al_2O_3 (CrAl_1 exchange vector), similar to chlorite in the transitional ultramafic lithologies between Atg-serpentinite and Chl-harzburgite (Padrón-Navarta et al., 2011). These high Cr contents suggest that metasomatic Chl-Di-Ol-rim derives from precursor Atg-serpentinite.

4.2.3 | Epidote

Representative epidote compositions are shown in Table S1. Epidote in equilibrium with chlorite and diopside in Grt-3 veins within Grand-metarodingite is iron-rich ($X_{\text{Ep}} = (\text{Ca}/[\text{X}]^2 \times \text{Fe}^{3+}/(\text{Si}/3)^3) = 0.60\text{--}0.78$). In the matrix of Type 2 Ep-metarodingite, epidote grains are zoned and have increasing values of pistacite component from the core ($X_{\text{Ep}} = 0.11\text{--}0.50$) to the rims ($X_{\text{Ep}} = 0.49\text{--}0.84$). Coarse epidote that replaced Grt-1 aggregates in Ep-metarodingite and epidote in Pyralps-metarodingite have similar composition with $X_{\text{Ep}} = 0.40\text{--}0.54$. In contrast, zoisite coexisting with epidote in Pyralps-metarodingite is Fe^{3+} -poor (0.1 a.p.f.u.; $X_{\text{Ep}} = 0.1$).

4.2.4 | Diopside

Diopside occurs in all the studied lithologies (Table S1). The X_{Mg} ranges between 0.90 and 0.96 in Grand- and Pyralps-metarodingites and spans to lower values in Ep-metarodingite (0.80–0.94) and the metasomatic reaction rims (0.85–0.99; Table S1). Jadeite+aegirine components are usually lower than 2 mol.%, except for grains in Pyralps-metarodingite which have up to 4 mol.% $\text{Jd} + \text{Aeg}$.

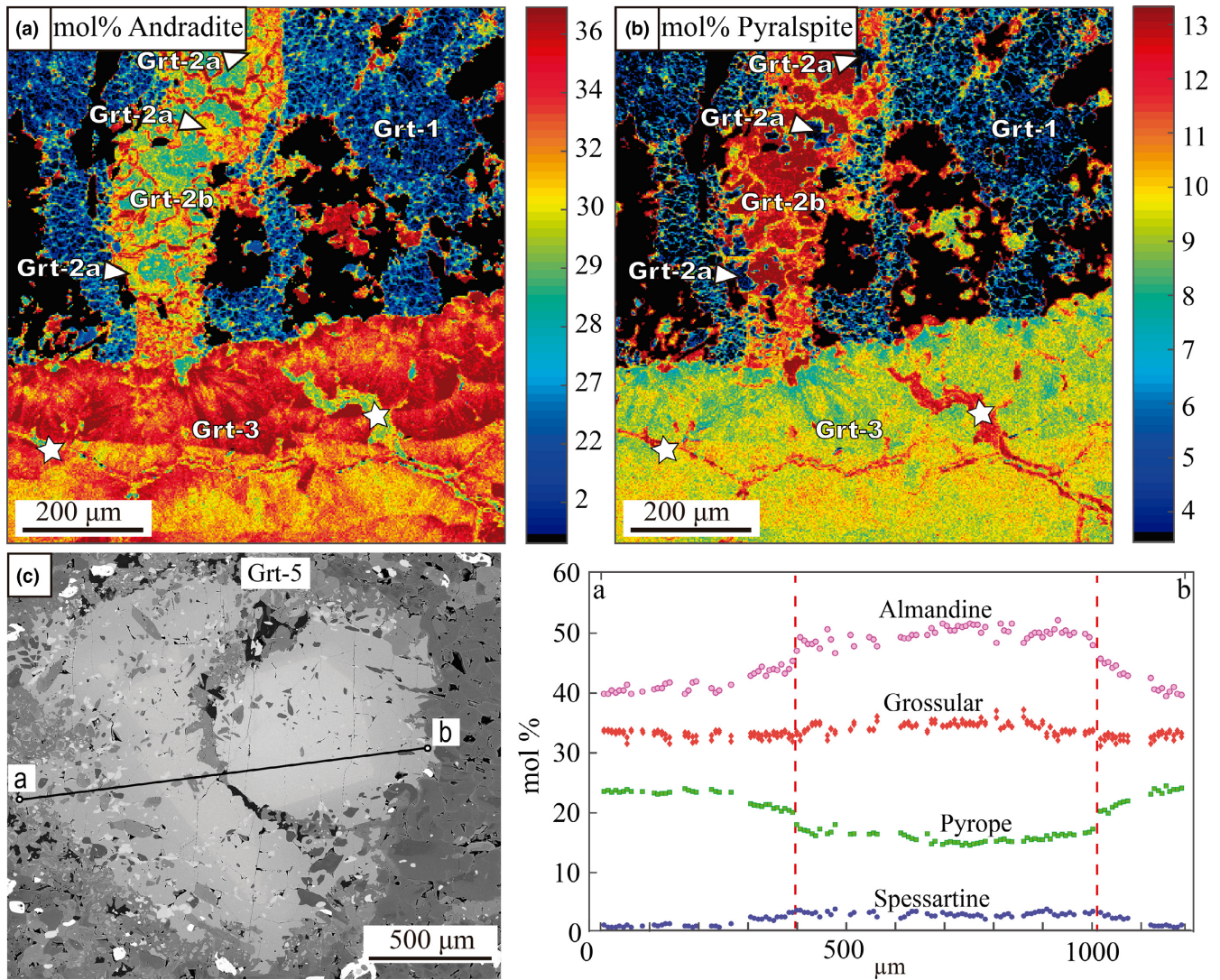


FIGURE 6 (a, b) Compositional maps of garnet in Grand-metarodingite (blue inset from Figure 4b, for the andradite (a) and pyralspite (pyrope+almandine+spessartine); (b) end-members. Grt-2a corresponds to the earliest scarce, andradite-rich and pyralspite-poor garnet formed in the first vein generation. White stars mark late veinlets with composition very similar to Grt-2b crosscutting the Grt-3 veins. Data obtained using XMapTools[®] (module Chem2D and external function Gar-StructForm-Fe³⁺; Lanari et al., 2014). (c) Compositional profile of Grt-5 in Pyralspite-metarodingite

4.2.5 | Amphibole

Amphibole structural formulae were calculated after Locock (2014). Composition shows a continuous, well-defined trend between tremolite and pargasite end-members (Table S1; Figure 7). The Amp-1 from Pyralspite-metarodingite ranges between tremolite ($X_{Mg} = 0.86–0.98$) and Mg-Hornblende ($X_{Mg} = 0.84–0.92$) compositions. Extensive late amphibolitization produced Amp-2 that plots within the pargasite field ($X_{Mg} = 0.72–0.85$). Amp-3, which rims Grt-5 in Pyralspite-metarodingite, has pargasite compositions with higher tschermakitic substitution ($X_{Mg} = 0.60–0.83$; Figure 7).

4.2.6 | Other minerals

Olivine in Chl-Di-Ol- metasomatic rims hosted by Atg-serpentinite presents $X_{Mg} = 0.91–0.92$, Ni = 0.005–0.007 a.p.f.u., and Mn = 0.004–0.005 a.p.f.u. (Table S1). These values are similar to those reported for clinopyroxene-tremolite-rich serpentinite (Padrón-Navarta et al., 2011). In the only Chl-Di-Ol-rim found in the Chl-harzburgite domain, the X_{Mg} range of olivine (0.90–0.91) and its Mn content (0.002–0.003 a.p.f.u.) are similar to those of olivine in the wall Chl-harzburgite, but the Ni (0.012–0.015 a.p.f.u.) contents are much higher than those reported in any other rock type from the Cerro del Almiraz massif.

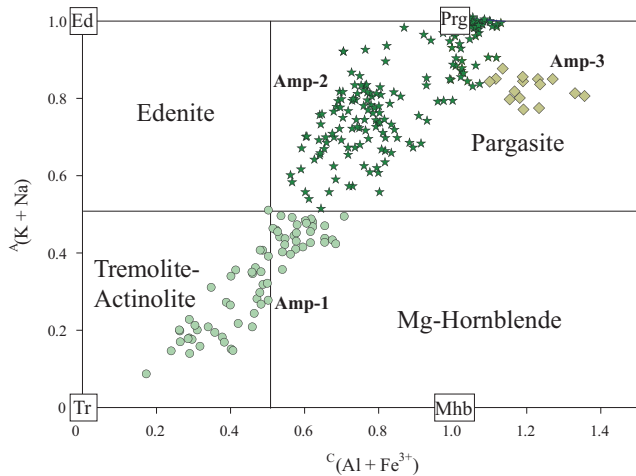


FIGURE 7 Amphibole compositional variation in the A(K+Na) versus C(Al+Fe³⁺) plot

Antigorite in Chl-Di-Ol-rim has Si = 1.88–1.90 and Al = 0.17–0.21 a.p.f.u. (Table S1), similar to Si and Al abundances in antigorite from clinopyroxene-tremolite-rich serpentinite and from transitional Chl-serpentinite (Padrón-Navarta et al., 2011).

Magnetite is rich in Cr in Grand-metaroddingite (up to 5.15 wt% Cr₂O₃) and in all the metasomatic reaction rims (up to 8.5 wt% Cr₂O₃). In contrast, magnetite in Ep-metaroddingite is Cr-free. Irrespective of the rock type, titanite has stoichiometric composition with low Al (0.12–0.41 a.p.f.u.) and F contents (below detection limit; Table S1).

4.3 | Bulk-rock compositions and oxidation state

Bulk-rock analyses (Table 3) and ternary diagrams in the ACFS system (Figure 8a) reveal significant compositional differences between metaroddingite types, their associated metasomatic rims and hosting ultramafic rocks. Type 1 Grand-metaroddingite is the CaO richest (25.7–30.3 wt%) and SiO₂ poorest (34.9–42.2 wt%) metaroddingite type. Compared to Type 1, Type 2 Ep-metaroddingite is CaO depleted (22.79–24.9 wt%) and SiO₂ enriched (43.2–44.1 wt%) and has similar MgO contents (6.3–6.7 wt% for both lithologies; Figure 8a). A stronger CaO depletion (~19 wt%), coupled to MgO enrichment (~9–12 wt%), characterizes Pyrals-metaroddingite (Figure 8a). Strong amphibolitization explains the high Na₂O contents (up to 1.8 wt%; Table 3) of Pyrals-metaroddingite and some Ep-metaroddingite samples. All the metasomatic reaction rims plot at intermediate compositions between those of metaroddingites and host ultramafic rocks. No clear

compositional differences in terms of major elements exist between Chl-blackwalls hosted in the Atg-serpentinite and Chl-harzburgite domains (Figure 8a).

Systematic differences in terms of bulk Fe³⁺/Fe_{Total} ratios exist between the studied lithologies (Figure 8b; Table 3). The highest values correspond to Grand-metaroddingite (Fe³⁺/Fe_{Total} = 0.66–0.83) and especially Ep-metaroddingite (Fe³⁺/Fe_{Total} = 0.76–0.89) from the Atg-serpentinite domain. Nonamphibolitized Ep-metaroddingite in Chl-harzburgite displays values within this range (Fe³⁺/Fe_{Total} = 0.78). However, Pyrals-metaroddingite has much lower Fe³⁺/Fe_{Total} (0.38–0.48). Amphibolitization of Ep-metaroddingites was coupled with a decrease in Fe³⁺/Fe_{Total} independently of the host (Figure 8b).

Chl-blackwalls have lower Fe³⁺/Fe_{Total} than the associated metaroddingites, and Fe³⁺/Fe_{Total} is higher in Chl-blackwalls from the Atg-serpentinite than from the Chl-harzburgite domains (Figure 8b). In contrast, Chl-Di- and Chl-Di-Ol- metasomatic rims have Fe³⁺/Fe_{Total} much higher than Chl-blackwalls, similar to values of Atg-serpentinites. The latter have Fe³⁺/Fe_{Total} notably higher than Chl-harzburgites (Figure 8b), in agreement with the results of Debret et al. (2015).

4.4 | Chemographic relationships and metamorphic reactions in metaroddingites

The chemographic analysis of metaroddingites (Figure 9) allows the extent of thermodynamic equilibrium achieved during their metamorphic evolution to be assessed, and deduction of the reactions that explain the main compositional changes in minerals and bulk-rocks.

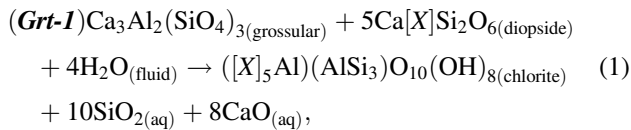
4.4.1 | Grandite-metaroddingite

In the ACFS system, the bulk-rock compositions of Grand-metaroddingites plot inside the space defined by Chl-Di and Grt-1 or Grt-2b or Grt-3 (Figure 9a). This indicates that the mineral assemblages of Grand-metaroddingites are in equilibrium. The chemographic relationships between the mineral and bulk-rock compositions of these rocks (Figure 9a) reflect: (a) the dominant modal abundance of garnet compared to chlorite and diopside (Table 1); (b) the different garnet compositions of Grt-1, Grt-2b and Grt-3 (Figure 5); and (c) the decrease of the diopside/chlorite modal ratio accompanied by the change from Grt-1 to -2b and -3. The most primitive bulk composition of Grand-metaroddingite plots close to the Grt-1—Di tie line and evolved towards the Grt-2b (or Grt-3)—Chl tie line with increasing metamorphic grade (Figure 9a). This change may have occurred through the reaction:

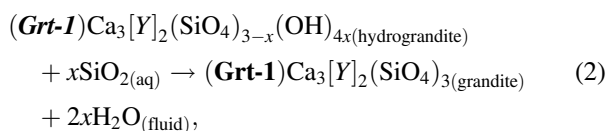
TABLE 3 Bulk-rock analyses of representative samples from the different metaroddingite types

Metaroddingite type	Grandite-metaroddingite	Epidote-metaroddingite		Amphibolitized epidote-metaroddingite		Pyralospite-metaroddingite
	Type 1	Type 2		Type 2		Type 3
Host rock	Atg-Serp.	Atg-Serp.	Chl-Harz.	Atg-Serp.	Chl-Harz.	Chl-Harz.
Sample wt%	AL14-64	AL14-17	AL14-86	AL14-26EA	AL14-143	AL 96-24B
SiO ₂	35.24	44.13	44.01	40.90	42.13	42.55
Al ₂ O ₃	16.49	14.57	15.44	17.10	15.42	17.70
TiO ₂	2.53	1.77	1.51	2.10	1.94	1.98
Fe ₂ O ₃ tot.	10.01	7.38	7.25	10.65	9.48	8.96
MnO	0.17	0.07	0.09	0.11	0.12	0.14
MgO	6.97	6.37	6.45	7.25	9.17	9.31
CaO	25.72	24.92	24.52	19.5	19.25	17.36
Na ₂ O	0.09	0.20	0.18	1.26	1.21	0.97
K ₂ O	0.020	0.00	0.02	0.59	0.33	0.44
P ₂ O ₅	0.40	0.2	0.19	0.20	0.24	0.20
LOI	2.31	0.39	0.33	0.34	0.69	0.40
Total	99.95	100.00	99.99	100.00	99.98	100.01
CaO*	24.40	24.27	23.87	18.84	18.46	16.71
FeOtot	9.00	6.64	6.52	9.58	8.53	8.06
FeO**	3.68	1.63	1.92	3.34	4.02	4.97
Fe ₂ O ₃	5.92	5.56	5.11	6.94	5.02	3.44
Total	99.54	99.81	99.78	99.63	99.53	99.46
A	0.24	0.21	0.21	0.24	0.20	0.21
C	0.26	0.25	0.25	0.20	0.20	0.18
F	0.12	0.08	0.09	0.12	0.14	0.15
S	0.38	0.46	0.46	0.44	0.45	0.46

CaO* = CaO-(3.33 P₂O₅) apatite Ca correction for pseudosections. FeO** analysed.



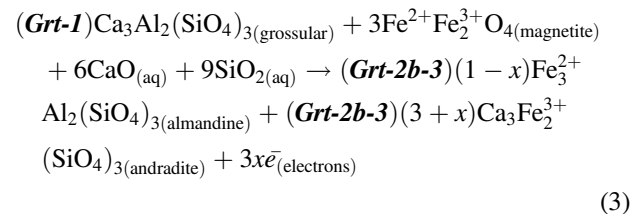
where Grt-1_{Grs} represents the grossular component in Grt-1 and [X] represents the FeMg₋₁ substitution in diopside and chlorite. This reaction, and the following ones, was balanced after the ideal stoichiometric composition of minerals. At least part of the fluid consumed in Reaction 1 might have come from the breakdown of the katoite component in the primitive hydrogranditic garnet (Grt-1) according to the simultaneous reaction:



where x , with a maximum possible range of 0–3, represents the SiH₄ substitution in Grt-1 (ranging between 0.06 and

0.18 in these rocks) and [Y] sums up the octahedral cations.

During the transformation of Grt-1 into Grt-2b or Grt-3 (Figure 6a,b), the observed decrease in the grossular and increase in the almandine and andradite contents can be explained by the breakdown of magnetite according to reaction:



where x ranges from 0 to 1. In the case of Grt-2b $x = 0$, thus the amount of almandine is the highest possible one, and the almandine/andradite ratio (1/3) is similar to that observed in Grt-2b (Alm₇₋₁₃ Adr₂₁₋₃₁ mol.%). In the case of Grt-3, an oxidizing agent is required to induce the partial oxidation of Fe²⁺ from magnetite and $x > 0$, (almandine/

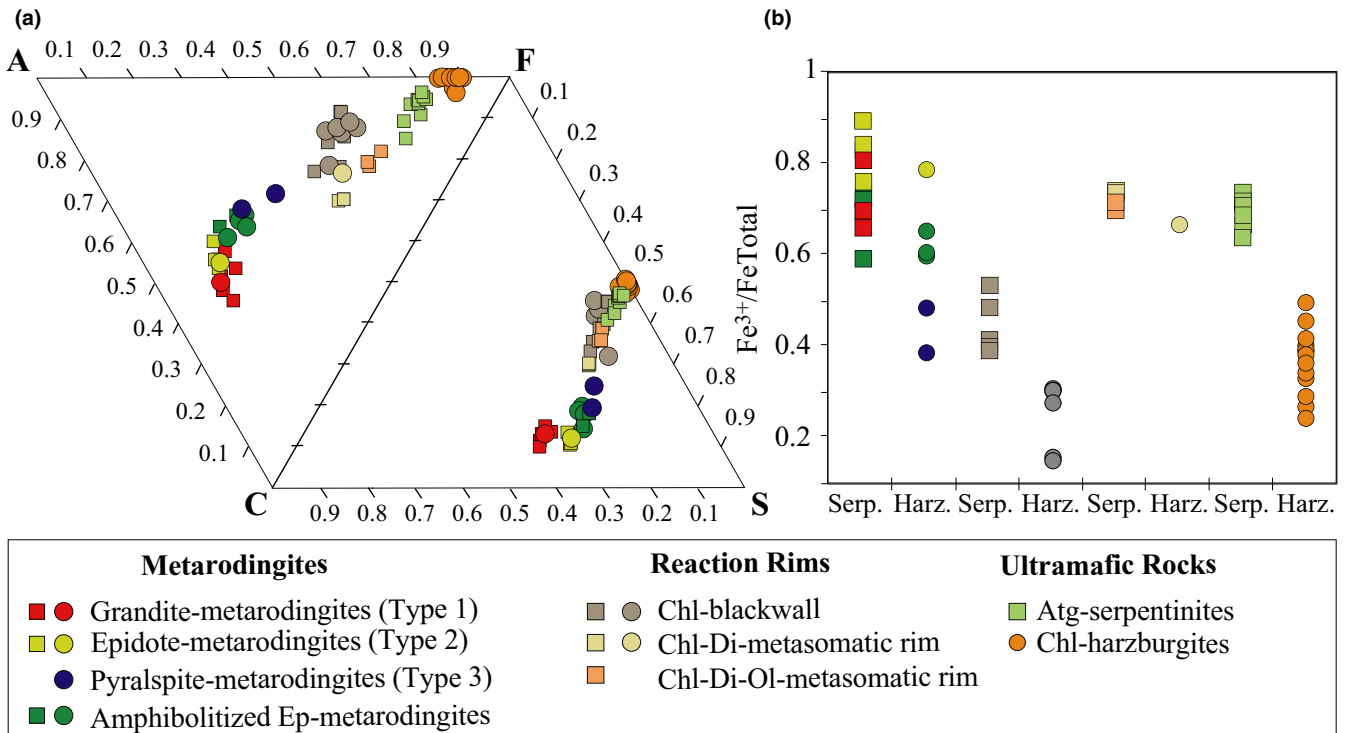
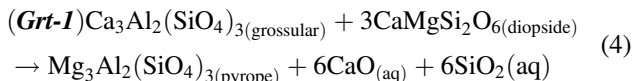


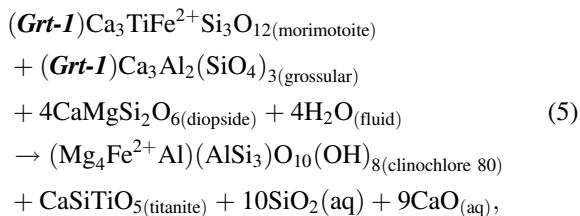
FIGURE 8 (a) ACFS diagram (Winkler, 1979) showing the bulk-rock compositional variation of metaroddingites, metasomatic reaction rims and hosting ultramafic rocks. Squares and circles indicate lithologies in the Atg-serpentinite and Chl-harzburgite domains respectively. A=Al₂O₃+Fe₂O₃-(Na₂O+K₂O); C=CaO-(3.33*P₂O₅); F=FeO+MgO+MnO; S=SiO₂. (b) Plot of bulk Fe³⁺/Fe_{Total} ratios for all the studied lithologies distinguished according to their ultramafic host domain

andradite ratio <1/3, Alm₂₋₈ Adr₃₁₋₅₃ mol.%). Therefore, contrary to the transformation of Gr-1 into Grt-2, the growth of Grt-3 implies an increase in the bulk-rock Fe³⁺/Fe_{Total} ratio.

The increase in the pyrope component of Grt-2b and Grt-3 (up to 7 mol.%) compared to Grt-1 is consistent with the diopside-consuming reaction:



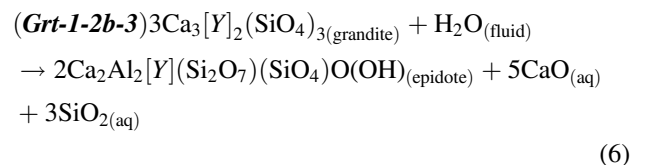
The growth of titanite, which coexists with Grt-2b and Grt-3, can be explained by Ti release from Grt-1 through the breakdown of the garnet morimotoite component:



This reaction contributes to the decrease in the bulk diopside/chlorite ratio (Figure 9a).

4.4.2 | Epidote-metaroddingite

The bulk-rock compositions of Ep-metaroddingites from both the Atg-serpentinite and Chl-harzburgite domains plot very close to the tie line epidote–diopside (Figure 9b), which are the main minerals in these rocks (Table 1). In agreement with petrographic observations, these compositions are also in equilibrium with low amounts of Grt-3 and chlorite (Figure 9b). The transformation of Grand into Ep-metaroddingites likely occurred by several independent reactions. The breakdown of grandite garnet (Grt-1, Grt-2b, Grt-3), which represents ~70 vol.% of Grand-metaroddingite, may have occurred by the hydration reaction:



where [Y] represents the Fe³⁺Al₋₁ substitution in the garnet granditic components and in epidote. The possible maximum range of [Y] consistent with stoichiometry spans from [Al₁] to [Fe³⁺_{0.33}Al_{0.67}].

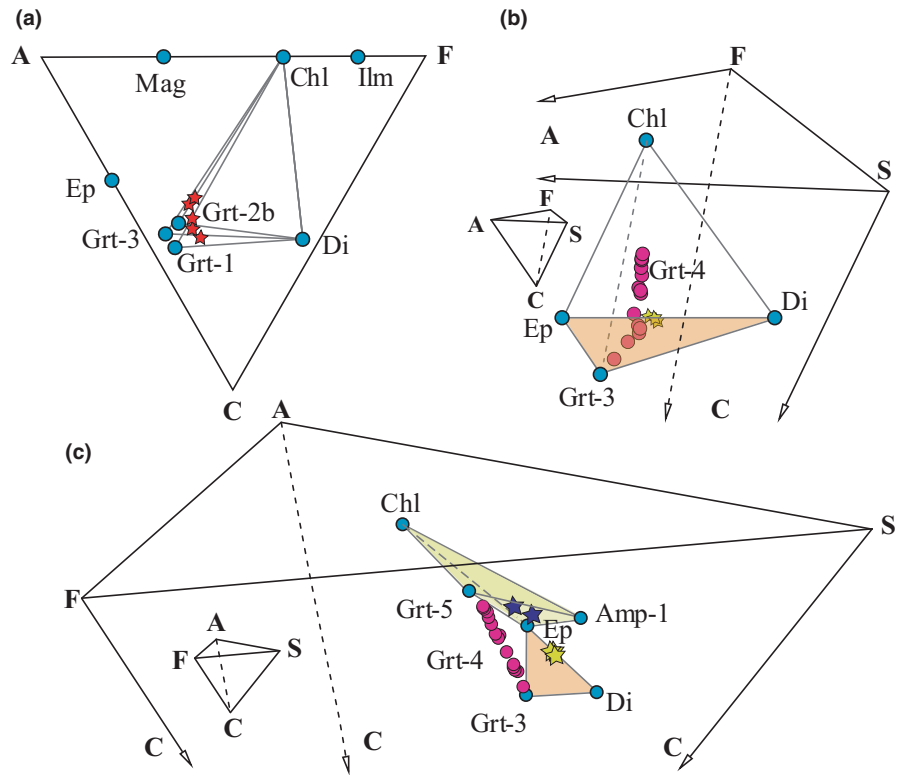
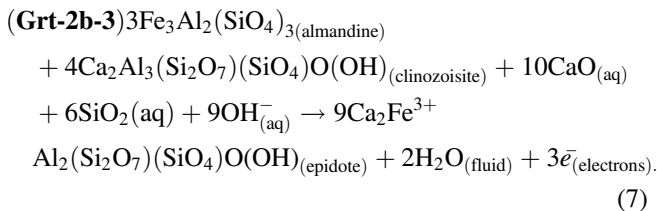
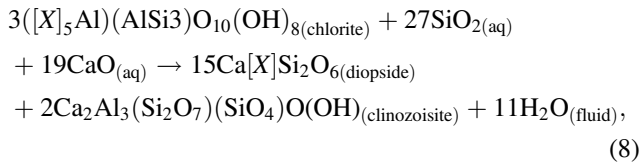


FIGURE 9 Chemographic relationships for the different metaroddingite types in the ACFS system. Bulk-rock compositions are indicated by stars and mineral compositions by dots. (a) Grandite-metaroddingite. (b) Epidote-metaroddingite. Purple dots represent the composition of Grt-4 grains in equilibrium in Ep-metaroddingite from the Chl-harzburgite domain. (c) Transition between Epidote- and Pyralpsite-metaroddingites (green tetrahedron) viewed in a different orientation compared to (b)

A concomitant reaction should have oxidized Fe^{2+} in the almandine component of Grt-2b and Grt-3 at water-saturated conditions:



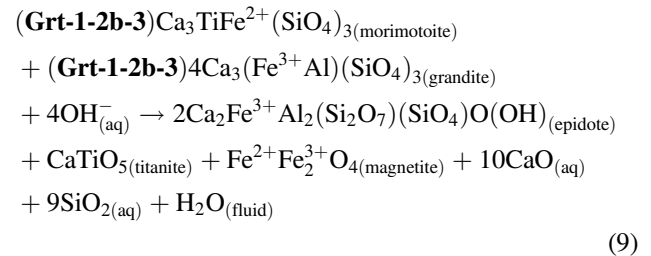
The observed breakdown of chlorite and growth of new diopside may have occurred through reaction:



where [X] represents the FeMg_{-1} substitution in chlorite and diopside.

The relative importance of Reactions 6–8 was controlled by the different chlorite/garnet ratios in precursor Grand-metaroddingite, which is richer in Chl towards the Chl-blackwall. However, an external source of water and an oxidizing agent (Reaction 7) must be invoked. Additionally, Ti in grandite-garnet was fully incorporated into titanite by Reaction 5. This may explain the higher amounts of titanite in Type 2 Ep-metaroddingites compared to Type 1.

Newly formed magnetite, texturally related to titanite, may have grown by reaction:



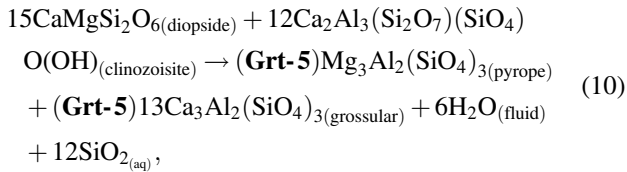
Ep-metaroddingites from the Chl-harzburgite domain have small recrystallized grains of Grt-4 (Figure 4e) with a particular compositional trend (Figure 5). In Figure 9c, these garnet compositions span the range between grandite garnet (Grt-3) and newly formed pyralpsite garnet (Grt-5) of Type 3 metaroddingite. Each of these compositions would set a different position of the Grt-apex of the Grt-Ep-Di-Chl tetrahedron that defines the mineral assemblage of Ep-metaroddingite (Figure 9b). Irrespective of the location of the Grt-apex, the bulk-rock compositions of Ep-metaroddingite plot within this tetrahedron, and hence, Grt-4 is in equilibrium with the main mineral assemblage.

4.4.3 | Pyralpsite-metaroddingite

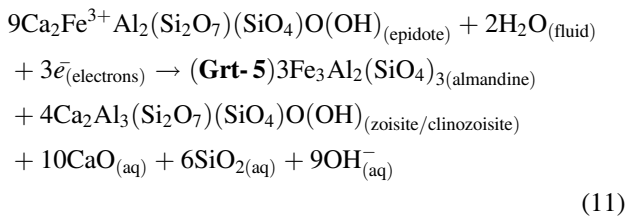
Transformation of Ep-metaroddingite into Pyralps-metaroddingite is marked by the crystallization of both pyralpsitic Grt-

5 and amphibole (Amp-1; green tetrahedron in Figure 9d). This metarodingite type is usually very poor in Chl and bulk composition analyses plot within the Chl-Ep-Grt-5-Amp-1 tetrahedron (Figure 9c).

The growth of Grt-5 can be explained by the following simultaneous reactions:

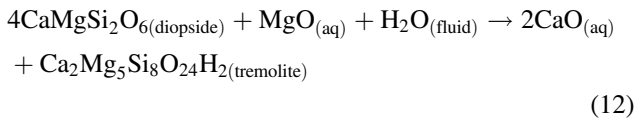


and



These reactions released fluid, CaO and SiO₂. Reaction 11 is the reverse of Reaction 7 and produces the reduction of Fe³⁺ in epidote to Fe²⁺ in almandine. This process may hence account for the strong drop in Fe³⁺/Fe_{Total} between Ep-metarodingite and Pyrls-metarodingite (Figure 8b).

Amphibole possibly formed by the diopside-consuming reaction:



which requires the addition of MgO and the loss of CaO in the metarodingite bulk chemical system. This compositional change between Ep- and Pyrls-metarodingites (Figures 8a and 9c) was probably enhanced by chemical potential gradients between metarodingites and host Chl-harzburgite.

4.5 | Thermodynamic modelling

Pseudosections for each metarodingite type have been calculated using *Perple_X* 6.7.6 (Connolly, 2009) in the system NCFMASHTO (Figure 10). According to chemographic analysis (Figure 9), thermodynamic equilibrium was reached in every metarodingite type. The reactive bulk composition considered in the calculations was obtained: (a) by subtracting from the bulk rock composition the amount of CaO in apatite (=3.33*P₂O₅ wt%), not relevant for the rock's phase relationships; and (b) by excluding bulk Na₂O contents as Na₂O concentrates only in amphibole (Amp-2 and Amp-3) formed during retrograde metasomatic amphibolitization and was not involved in the

prograde metamorphic path of the rocks. We used the internally consistent thermodynamic database of Holland and Powell (1998, revised version of 2002) and the following solid solution models: orthopyroxene, clinopyroxene (Holland & Powell, 1996); olivine, spinel, saphirine, staurolite, chloritoid (Holland & Powell, 1998); chlorite (Holland, Blanford, & Stein, 1998); epidote (Holland & Powell, 2011); antigorite (Padrón-Navarta et al., 2013); amphibole (Dale, Holland, & Powell, 2000); garnet (White, Powell, & Holland, 2007); magnetite ulvospinel (Andersen & Lindsley, 1988); plagioclase (Newton & Haselton, 1981); pumpellyite (Massonne & Willner, 2008). Ideal solution models were adopted for talc, brucite, anthophyllite, wustite, ilmenite, clinohumite, carpholite and sudoite. Zoisite was considered as a pure phase. The CORK equation of state for H₂O–CO₂ fluids (Holland & Powell, 1998) was used, although fluids have been considered pure H₂O.

The lack of suitable solid solution models may explain some inconsistencies between the observed and predicted phase compositions. This is especially the case of garnet, whose solution model does not consider H₂O- and Ti-rich end-members (Ca₃Al₂OH₁₂ and Ca₃[TiFe²⁺]₃Si₃O₁₂, respectively). Thus, excess Ti in the form of low amounts (<4 vol.%) of ilmenite—not always observed in the rocks—is commonly predicted by the calculations (e.g., ilm in the blue-labelled fields in Figure 10a). Moreover, the exclusion from calculations of the CaO contents of these end-members results in an overestimation (<10 mol.%) of the calculated amounts of the grossular component.

4.5.1 | Grandite-metarodingite

The *P–T* pseudosection for a representative Type 1 Grand-metarodingite (A114-64 without Na₂O component; Table 3) is shown in Figure 10a. The assemblage observed in this rock (Grt+Chl+Ttn, labelled in blue) is stable at temperatures and pressures of 560–675°C and 9–20 kbar, respectively. These conditions are constrained by the stability of epidote at low-*P* and low-*T*, rutile at high-*P*, and clinopyroxene at low-*P* and high-*T*, which are not present in this rock. The calculated composition of garnet (Grs₆₂₋₆₄ Adr₂₂₋₃₃ Pyrls₁₃₋₁₆) matches that of Grt-2b (Table 2; Figure 5), and the modal amounts of minerals (70–74 vol.% Grt; 23 vol.% Chl; 4 vol.% Ttn) are also consistent with those of the rock (Table 1).

Grossular-rich and pyrlspite-poor garnet, similar to Grt-1, is stable at <7 kbar and 200–400°C and coexists with clinopyroxene, chlorite, magnetite, and titanite (Figure 10a, green label), coinciding with the observed assemblage in equilibrium with Grt-1. Epidote, however, is also predicted in this field (7–8 vol.%), but this mineral did not crystallize in Type 1 metarodingite. Moreover, no garnet composition equivalent to Grt-3 is predicted to be stable in the whole *P–T* field of this pseudosection.

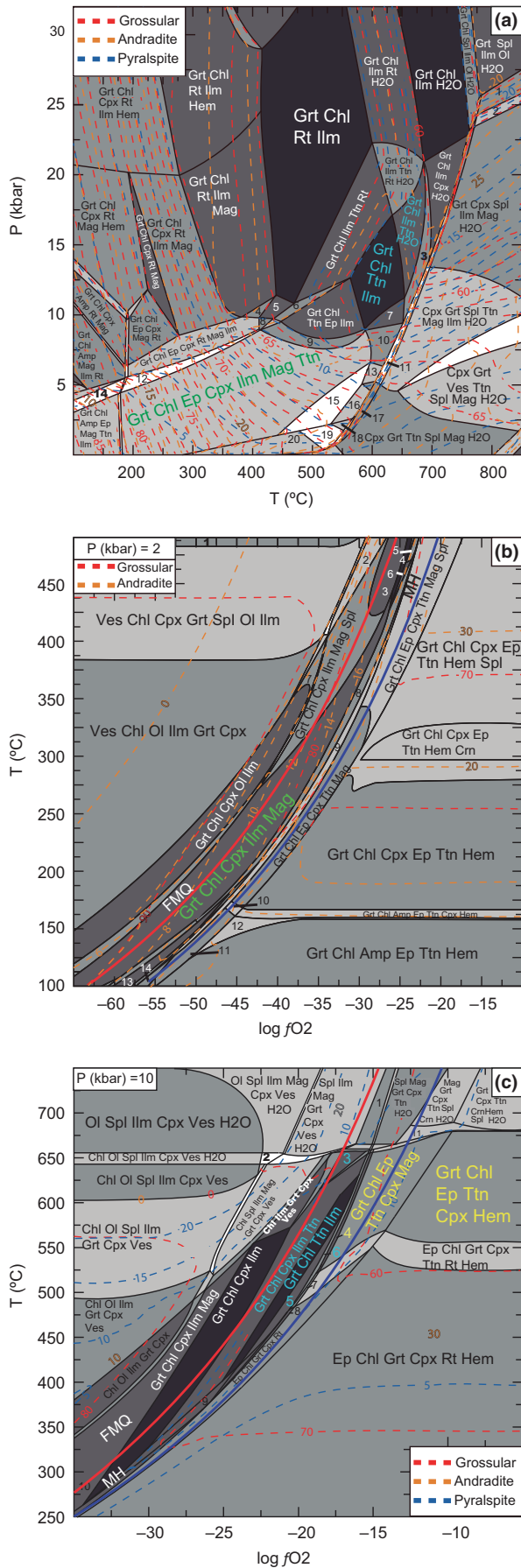


FIGURE 10 P - T - $\log fO_2$ constraints from thermodynamic modelling using *Perple_X* for Type 1 Grand-metaroddingite (sample A114-64 bulk-rock composition; Table 3). (a) P - T pseudosection. The blue-labelled assemblages are those observed in the rock. At these conditions, the Grt-2b composition is stable, as indicated by isopleths (dashed lines) for the grossular, andradite and pyrralspite (pyrope+almandine+spessartine) garnet end-members. Grt-1 composition is stable at lower P - T conditions (green-labelled assemblage), where it coexists with epidote (absent in the rock). (b) T - $\log fO_2$ pseudosection at 2 kbar. Grt-1 composition and the observed coexisting mineral assemblage are stable in the green-labelled field up to $\sim 325^\circ\text{C}$. Stability of this assemblage is limited by that of olivine and vesuvianite at low $\log fO_2$ conditions and by stability of epidote at high $\log fO_2$. (c) T - $\log fO_2$ pseudosection at 10 kbar. Grt-2b composition (pyrralspite >10 mol.%) and the observed coexisting mineral assemblage are stable in the blue-labelled fields at $>400^\circ\text{C}$ and $\log fO_2 > -25$. Grt-3 composition (andradite >30 mol.%) and the observed coexisting mineral assemblage (including up to 16 vol.% epidote) are stable in the yellow-labelled fields at $>550^\circ\text{C}$ and $\log fO_2 > -15$. Thick red and purple lines show the conditions of FMQ and MH buffers of oxygen fugacity respectively. Stable assemblages in the numbered fields are shown in Table S2

Besides pressure and temperature, oxygen fugacity should also have changed during the metamorphic evolution of Grand-metaroddingite, as evidenced by the variation in the bulk-rock $\text{Fe}^{3+}/\text{Fe}_{\text{Total}}$ ratio produced by the crystallization of Grt-3 (Reaction 3). Isobaric T versus $\log fO_2$ pseudosections for the same Grand-metaroddingite sample calculated at different pressures (Figure 10b,c) show that the original rodingitic assemblage (Grt+Chl+Cpx+Mag+Ilm) and the observed composition of Grt-1 ($\text{Gr}_{\text{S}64-84}$ $\text{Adr}_{\text{S}5-19}$ $\text{Pyrr}_{\text{S}0-3}$) are stable at 2 kbar, 150 – 325°C and $\log fO_2$ ranging from -55 to -35 , equivalent to the fayalite-magnetite-quartz redox buffer (FMQ) ranging from -2 to $+3$ (Figure 10b). These fO_2 conditions are well constrained by the calculated Grt-1 composition and the lack of epidote, olivine, and vesuvianite in the observed mineral assemblage.

Grt-2b is stable at a minimum pressure of 10 kbar. At this pressure, the typical assemblage (Grt+Chl±Cpx+Ttn (+Ilm)) coexisting with Grt-2b is stable at 350 – 650°C and $\log fO_2$ of -25 to -15 , equivalent to FMQ ranging from -1 to $+3$ (Figure 10c). At these conditions, the model predicts several petrographic and compositional features of Type-1 Grand-metaroddingite, such as the stability of titanite, the lack of magnetite, the progressive decrease of diopside abundance, and the composition of garnet ($\text{Gr}_{\text{S}65-70}$ $\text{Adr}_{\text{S}20-30}$ $\text{Pyrr}_{\text{S}12}$), which is very similar to that of Grt-2b ($\text{Gr}_{\text{S}42-61}$ $\text{Adr}_{\text{S}21-31}$ $\text{Pyrr}_{\text{S}10-13}$). At 10 kbar, epidote-bearing assemblages with garnet compositions ($\text{Gr}_{\text{S}<60}$ $\text{Adr}_{\text{S}>30}$ $\text{Pyrr}_{\text{S}<10}$) equivalent to those of Grt-3 are stable at $\log fO_2 > -19$, over and above the magnetite-hematite redox buffer

(MH), and between 525°C (below which rutile is stable) and 675°C (above which spinel is stable; Figure 10c). The maximum pressure at which grandite-garnet-bearing assemblages are stable cannot be constrained by isobaric T versus $\log f_{O_2}$ phase diagrams.

4.5.2 | Epidote-metarodingite

The thermodynamic model shown in Figure 10c predicts the stability of the mineral assemblages of Ep-metarodingite (yellow-labelled fields), but the calculated modal proportions (4–16 vol.% epidote and 2–4 vol.% clinopyroxene) strongly differ from the real ones (~50–55 vol.% epidote and ~35–40 vol.% clinopyroxene). Thus, increasing oxygen fugacity alone ($\log f_{O_2} = -20$ to -5) cannot explain the complete transformation of Grand-metarodingite into Ep-metarodingite. Bulk compositional differences between these metarodingite types (Figure 8a) and Reactions 6 and 8 instead support that the chemical potentials of SiO_2 (μ_{SiO_2}) and CaO (μ_{CaO}) acted, together with pressure,

temperature and f_{O_2} , as independent thermodynamic variables during this transformation (Figure 11a).

To investigate this hypothesis, a μ_{SiO_2} – μ_{CaO} pseudosection was calculated for the same Grand-metarodingite bulk composition (A114-64; Table 3) at H_2O -saturated conditions for 16 kbar and 625°C (Figure 11a). These P – T values are consistent with the stability conditions of Grt-2b in Grand-metarodingites (blue-labelled fields in Figure 10a), which form boudins partially transformed into Ep-metarodingite in the Atg-serpentinite domain (Figure 2d). Fields labelled in red and yellow in Figure 11a match very well the assemblages of Grand- (Grt-2b-Chl-Ttn) and Ep- (Ep-Cpx-Ttn-Grt-3) metarodingites respectively. The predicted garnet compositions, indicated by isopleths (Grs₆₅ Adr₂₅ Pyrs₁₀ for Grt-2b and Grs₅₀₋₆₀ Adr₃₃ Pyrs₁₀₋₂₀ for Grt-3), are also consistent with those of the rocks (Figure 5). Transformation from Grand- to Ep-metarodingites was thus enhanced by decreasing μ_{CaO} (-708 to -725 kJ/mol) and increasing μ_{SiO_2} (-884 to -860 kJ/mol) values. Moreover, the bulk-rock

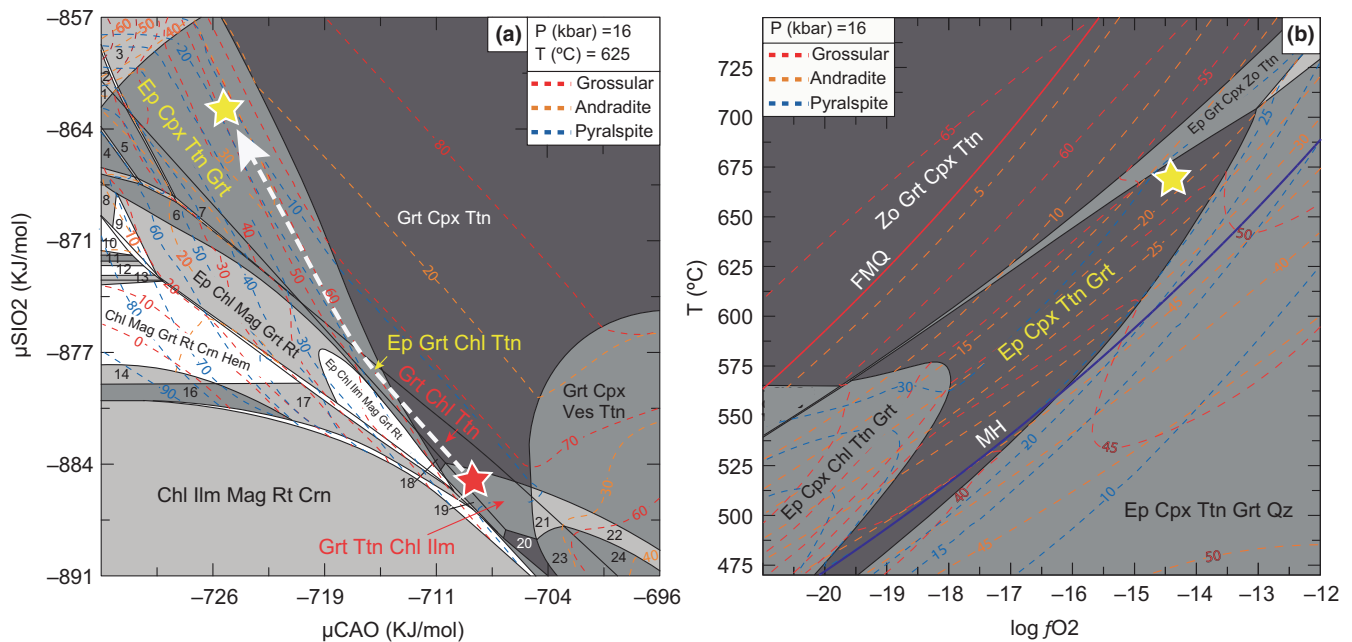


FIGURE 11 Thermodynamic modelling using Perple_X for constraining the transition from Type 1 to Type 2 metarodingites and for the stability conditions of Type 2, Ep-metarodingite. (a) μ_{SiO_2} – μ_{CaO} pseudosection for the bulk-rock composition of a Grand-metarodingite sample (A114-64; Table 3) at constant 16 kbar and 625°C and H_2O saturation conditions. It reproduces the transition from Grand-metarodingite to Ep-metarodingite (white-dashed arrow). The red star, red-labelled assemblages and the corresponding garnet composition defined by isopleths (dashed lines) are those of Grand-metarodingite with Grt-2b. Transition to the typical mineralogy of Ep-metarodingite (yellow-labelled fields) and stable Grt-3 composition (yellow star) is enhanced by μ_{CaO} decrease and μ_{SiO_2} increase. The predicted bulk-rock composition at the yellow star conditions ($SiO_2 = 44.10$; $TiO_2 = 2.13$; $Al_2O_3 = 13.93$; $Fe_2O_3 = 5$; $FeO = 3.11$; $MnO = 0.14$; $MgO = 5.89$; $CaO = 24.79$; $H_2O = 0.90$ wt%) compares well with the analysed composition of an Ep-metarodingite from the Atg-serpentinite domain (sample A114-17; Table 3). (b) T – $\log f_{O_2}$ pseudosection calculated at constant 16 kbar and H_2O saturation conditions for the bulk-rock composition obtained by Perple_X at the yellow star conditions in (a). The Ep-metarodingite assemblage (yellow label) is stable over a wide temperature range and at $\log f_{O_2}$ higher than Grand-metarodingite. Garnet isopleths indicate that, at the conditions marked by the yellow star, stable Grt-4 has the lowest almandine-pyrophe and the highest grossular-andradite contents. Thick red and purple lines show the conditions of FMQ and MH buffers of oxygen fugacity respectively. Stable assemblages in the numbered fields are shown in Table S2

composition predicted for Ep-metaroddingite at the stability conditions marked by the yellow star in Figure 11a (i.e., those corresponding to the observed composition of Grt-3) compares very well with the composition of a real Ep-metaroddingite (sample A114-17; Table 3) from the Atg-serpentinite domain.

The possible influence of fO_2 in the stability of Ep-metaroddingite assemblages is represented in an isobaric T versus fO_2 pseudosection (Figure 11b) for the bulk composition of sample A114-17 (Table 3). As Ep-metaroddingite bodies with identical mineral assemblages occur both in Atg-serpentinite and Chl-harzburgite domains, the pressure for modelling (16 kbar) was chosen in agreement with the minimum pressure at which the assemblages of both Atg-serpentinite and Chl-harzburgite equilibrated (Padrón-Navarta et al., 2012). In Ep-metaroddingite, the stability conditions of the assemblage Ep+Cpx+Ttn+Grt (in yellow; Figure 11b) span from 475 to 700°C for a wide range of $\log fO_2$ between -20 and -13.2 , equivalent to MH ranging from -2 to -1 . Within this field, isopleths indicate that Grt-4 (Figure 5) with composition Grs₅₀₋₅₅ Adr₁₅₋₂₀ Pyrals₂₅₋₃₀ is stable at $>650^\circ\text{C}$ and $\log fO_2 = -15$ to -13 (yellow star in Figure 11b). Modal proportions within this field (32–42 vol.% epidote, 47–53 vol.% clinopyroxene, 2 vol.% garnet, 4 vol.% titanite) also match those of Type 2 Ep-metaroddingite. These results demonstrate that Grt-4-bearing assemblages in Ep-metaroddingite formed at temperatures within the Chl-harzburgite stability field and beyond Atg breakdown in serpentinite.

4.5.3 | Pyralpitemetaroddingite

Phase relations show that neither Grt-5 nor tremolite-rich amphibole, both typical of Pyralpitemetaroddingite, are stable at conditions modelled in the pseudosection of Figure 11b. The compositional differences between Type 2 and Type 3 metaroddingites (Figure 8a) and metamorphic reactions 10–12 support that the chemical potentials of MgO (μMgO) and CaO (μCaO) were independent thermodynamic variables, jointly with pressure, temperature and fO_2 , during the transformation of Ep-metaroddingite into Pyralpitemetaroddingite. Another important observation is that a significant chemical transfer between the metaroddingites and the ultramafic host is indeed observed in the complex sequence of the metasomatic reaction rims that equally attest for spatial (and temporal) variations in μMgO and μCaO . This variation in chemical potentials along cm- to m-scale reflects the time-dependent (diffusional) process of reequilibration between the two contrasting bulk chemical compositions (mafic and ultramafic in origin) induced by fluid-mediated dissolution-precipitation processes. This process allows the relaxation of the initial stepped chemical potential gradients by effective chemical diffusion (by advection in the

aqueous fluid) thus justifying the use of μMgO and μCaO as independent thermodynamic variables.

We thus calculated a μMgO – μCaO pseudosection (Figure 12a) for the Ep-metaroddingite bulk composition corresponding to the yellow star in Figure 11b, that is, at 16 kbar and 660°C , (i.e., well within the stability field of Chl-harzburgite), $\log fO_2 = -14.5$ and H_2O saturation conditions.

Fields labelled in yellow and blue colours match very well the assemblages of Ep-(Ep+Cpx+Ttn+Grt; hosted in Chl-harzburgite) and Pyralpitemetaroddingites, respectively (Figure 12a). The μCaO and μMgO values corresponding to the yellow star are those established by Perple_X for the stability conditions of Grt-4 (yellow star in Figure 11b). The predicted garnet compositions (indicated by isopleths) in each field are also consistent with those of the corresponding rock type and in particular with the decrease in the andradite and grossular end-members and increase of pyralpitemetaroddingite from Grt-4 (Grs₃₅₋₅₂ Adr₅₋₂₀ Prp₆₋₂₃ Alm₁₃₋₃₀ Sps₃₋₁₀) in Ep-metaroddingite to Grt-5 (Grs₁₇₋₃₅ Adr₂₋₇ Prp₁₀₋₃₀ Alm₃₅₋₅₀ Sps₁₋₁₀) in Pyralpitemetaroddingite. Therefore, as indicated by the white arrow in Figure 12a, the transformation from Type 2 into Type 3 metaroddingites was enhanced by decreasing μCaO (-726 to -735 kJ/mol) and increasing μMgO (-630 to -626 kJ/mol). Additionally, the predicted bulk-rock composition of Pyralpitemetaroddingite at the conditions marked by the blue star in Figure 12a compares well with that of the Pyralpitemetaroddingite sample A196-24B (Table 3). The only minor discrepancies in Al_2O_3 and MgO may be due to the incomplete removal of chlorite-rich zones during the preparation of this sample.

Figure 12b shows a P – T pseudosection for a representative Type 3 Pyralpitemetaroddingite (A196-24B; Table 3). The mineral assemblages of Pyralpitemetaroddingite are stable at 635 – 740°C and 7 – 18.5 kbar (blue labels in Figure 12b). The main difference between the observed (Ep+Amp+Grt+Rt+Chl) and predicted (Ep+Amp+Grt+Rt+Chl+Cpx) mineral assemblages consists in the expected stability of Cpx (<5 vol.%) at $>660^\circ\text{C}$. Although not present in all Pyralpitemetaroddingites, relicts of diopside have been detected in some of these samples. Zoisite is observed in the studied rocks, but the model predicts that this phase is stable at lower pressures than those corresponding to the actual garnet compositions (Figure 12b). However, the relative stability of epidote and zoisite is highly conditioned by slight shifts of oxygen fugacity, and we cannot exclude that the analysed $\text{Fe}^{3+}/\text{Fe}_{\text{Total}}$ ratio used in calculations was affected by late amphibolitization.

Garnet isopleths constrain the conditions of formation of Grt-5 almandine-rich cores (Alm₄₈₋₄₉ Prp₁₇₋₁₈ Grs₂₆₋₂₈) in Type 3 Pyralpitemetaroddingites at 640 – 650°C and 11 – 16 kbar (Figure 12b), whereas pyrope-richer rims (Alm₃₇₋₄₂ Prp₂₂₋₃₀ Grs₂₇₋₃₀) formed at 660 – 684°C and 15.5 – 18.5 kbar. The

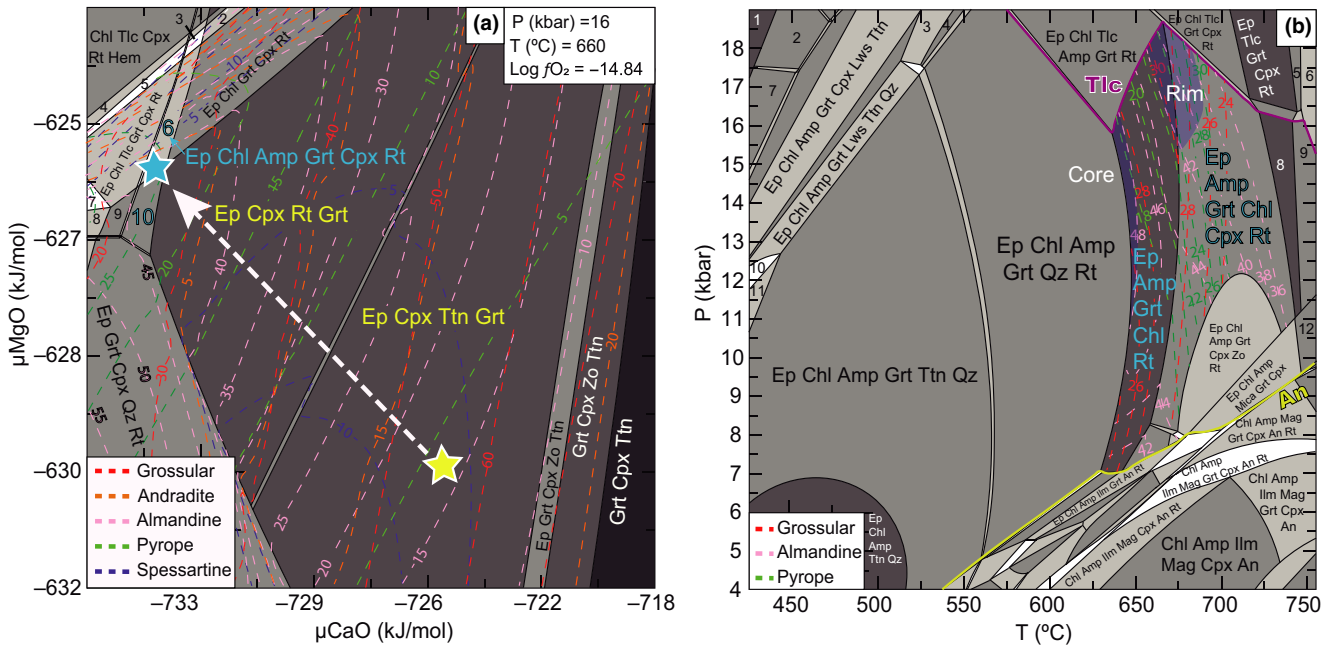


FIGURE 12 Thermodynamic modelling using *Perple_X* for constraining the transition from Type 2 to Type 3 metarodinites and the stability conditions of Type 3 Pyralite-metarodinite. a) μMgO - μCaO pseudosection at constant 16 kbar, 660°C and H_2O saturation conditions for the Ep-metarodinite bulk-rock composition and $\log f_{\text{O}_2}$ value estimated by *Perple_X* for the yellow star in Figure 11b ($\text{SiO}_2 = 44.52$; $\text{TiO}_2 = 1.79$; $\text{Al}_2\text{O}_3 = 14.70$; $\text{O}_2 = 0.36$; $\text{FeO} = 6.70$; $\text{MnO} = 0.07$ wt%). This model reproduces the transition from Ep-metarodinite (yellow-labelled assemblages) to Pyralite-metarodinite (blue-labelled assemblages). μCaO and μMgO values marked by the yellow star correspond to those of the yellow star in Figure 11b. At these conditions, the calculated garnet composition matches that of Grt-4 grains from Ep-metarodinites hosted in Chl-harzburgites with the lowest almandine, pyrope and the highest grossular contents. Change in garnet composition along the white arrow matches the observed compositional range of Grt-4 (Figure 5). Transition to the typical mineralogy of Pyralite-metarodinite (blue-labelled fields) and the stable Grt-5 composition (blue star) is enhanced by μCaO decrease and μMgO increase. The predicted bulk-rock composition at the blue star conditions ($\text{SiO}_2 = 43.6$; $\text{TiO}_2 = 1.75$; $\text{Al}_2\text{O}_3 = 14.4$; $\text{O}_2 = 0.35$; $\text{FeO} = 6.56$; $\text{MnO} = 0.07$; $\text{CaO} = 17.80$; $\text{MgO} = 12.37$; $\text{H}_2\text{O} = 2.89$ wt%) compares well with the analysed composition of a Pyralite-metarodinite from the Chl-harzburgite domain (sample A196-24B; Table 3). (b) P - T pseudosection for Type 3 Pyralite-metarodinite at H_2O saturation conditions (sample A196-24A bulk-rock composition excluding Na_2O ; Table 3). The blue-labelled assemblages are those observed in the rock. Garnet isopleths (dashed lines) constrain the stability conditions for the Grt-5 cores and rims (blue shaded areas). Peak P - T conditions were reached by rims at 660–684°C and 15.5–18.5 kbar. Stable assemblages in the numbered fields are shown in Table S2

latter conditions set the peak pressure and temperature for the prograde evolution of metarodinites at Cerro del Almiraz.

Precise oxygen fugacity conditions for Pyralite-metarodinite could not be independently determined. However, a $\log f_{\text{O}_2}$ value of -14.84 was assumed for the pseudosection of Figure 12a after the stability conditions deduced for Ep-metarodinite in Chl-harzburgite (yellow star in Figure 11b). At this $\log f_{\text{O}_2}$ value, the stability conditions of the Pyralite-metarodinite assemblages can also be deduced (blue fields in Figure 12a), and thus, it is assumed that these oxygen fugacity conditions are valid for these rocks.

5 | DISCUSSION

The Cerro del Almiraz metarodinites underwent a complex tectono-metamorphic evolution including peak

metamorphism at eclogite facies conditions. The deduced P - T path has been summarized in Figure 13, in which the different transformation stages of metarodinites were superposed on a representative pseudosection for the enclosing serpentinites. Variation in the amount of H_2O coexisting with the serpentinite and Chl-harzburgite stable assemblages and their possible correlation with metamorphic changes in the hosted metarodinites are also shown (see discussion below).

5.1 | Seafloor origin of rodingites

Rodingitic metastable assemblages are preserved in the less deformed Grand-metarodinites (Figure 2a). Despite the lack of relicts of igneous rocks, an igneous mafic protolith of metarodinites is indicated by: (a) preserved igneous porphyritic textures (Figure 4a,c); (b) garnet pseudomorphs after plagioclase (Figure 4a; similar to those reported by

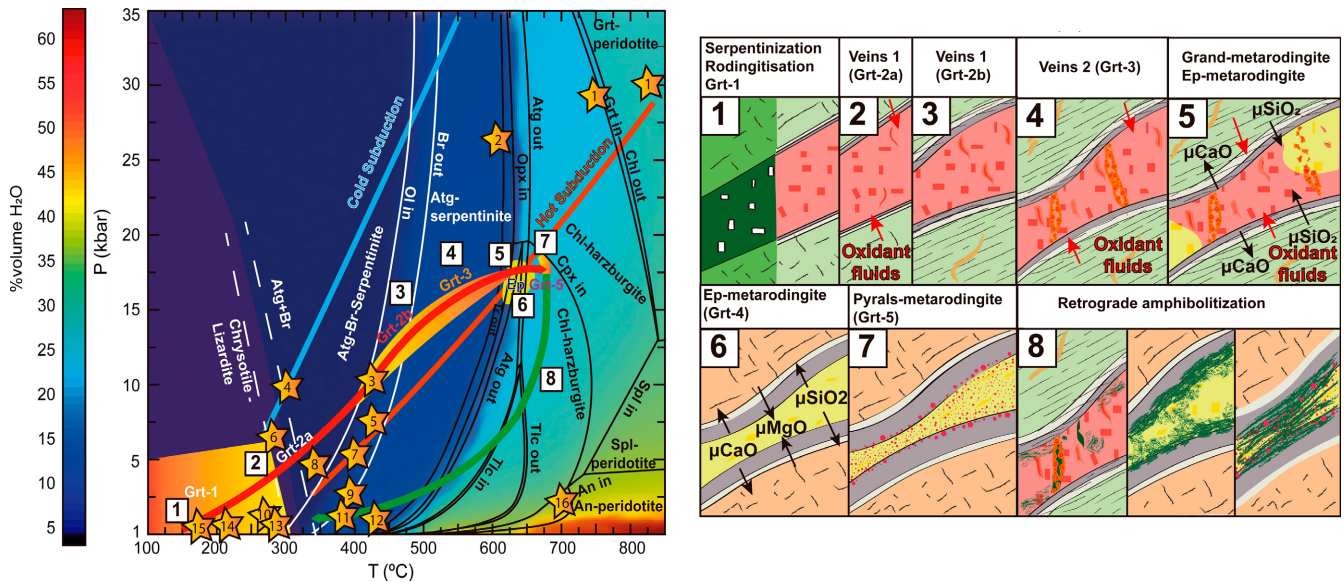


FIGURE 13 Summary of the proposed P - T path for the Cerro del Almiraz metarodingites superposed on a P - T pseudosection calculated for a representative Atg-serpentine. Background colours (see chart) show increasing H_2O amounts released with temperature due to prograde dehydration reactions. The stability limits of chrysotile and lizardite are taken from Evans (2004). Numbers in the white squares mark the approximate formation conditions for the different garnet generations and metarodingite types shown in the sketch diagrams below: 1: Rodingitization; 2: Probable Grt-2a formation conditions during chrysotile-lizardite breakdown; 3: Grt-2b formation; 4: Grt-3 formation during brucite breakdown; 5: Growth of Ep-metarodingite due to progressive Atg breakdown; 6: Complete Ep-metarodingite transformation; 7: Growth of Grt-5 rim; 8: Retrograde amphibolitization. Orange stars represent the estimated stability conditions of different rodingites and metarodingites in literature that are shown for comparison. 1: Cima di Gagnone (Cannaò, Agostini, Scambelluri, Tonarini, & Godard, 2015; Evans & Trommsdorff, 1978; Evans et al., 1979), 2: Zermat Saas (Barnicoat & Fry, 1986; Ferrando et al., 2010; Li et al., 2004; Zanoni et al., 2016), 3: Meliatic Bôrka Nappe (Li, Putiš, Yang, Koppa, & Dyda, 2014), 4: Kamuikotan Tectonic Belt (Banno, 1986; Katoh & Niida, 1983), 5: Tianshan (Li et al., 2007), 6: Cape San Martín (Franciscan Complex; Coleman, 1967; Ernst, 2011; Terabayashi & Maruyama, 1998), 7: Val Malenco (Berger & Bousquet, 2008; Puschnig, 2002), 8 and 11: JM Asbestos mine (Normand & Williams-Jones, 2007), 9: Abitibi belt (Schandl et al., 1989), 10: Bou Azzar (Leblanc & Lbouabi, 1988), 12: Appalachian Piedmont (Mittwede & Schandl, 1992), 13: Cassiar (O'Hanley et al., 1992), 14 and 15: Mid Atlantic ridge (Frost et al., 2008; Honnorez & Kirst, 1975), 16: Paddy-Go-Easy Pass (Frost, 1975)

Frost et al., 2008), of diopside (with exsolved inclusions of magnetite and ilmenite) after clinopyroxene (see also Ferrando et al., 2010) and of Chl+Di+Mag+Ilm after olivine (e.g., Früh-Green et al., 2003); and (c) the presence of Cr-rich magnetite, coexisting with Grt-1, possibly derived from igneous Cr-spinel.

Metarodingites in Cerro del Almiraz are associated with Atg-serpentinites or their dehydration products, that is, Chl-harzburgites (Figure 1b). Rodingitization of igneous mafic rocks is always simultaneous with serpentinization of host peridotites (Coleman, 1963; O'Hanley, 1996). Rodingites are typically considered to form by Ca-metasomatism at low SiO_2 activities at the seafloor (Bach & Klein, 2009; Coleman, 1967; Frost, 1975; O'Hanley et al., 1992; Schandl et al., 1990). The Cerro del Almiraz ultramafic rocks were originally serpentinized at $\sim 200^\circ C$ at the seafloor (Alt et al., 2012; Marchesi et al., 2013). Simultaneous rodingitization of mafic rocks is indicated by the low temperature (150 – $325^\circ C$) and low pressure (2 kbar) calculated for the stability of the most primitive assemblage preserved in Grand-metarodingite (Grt-1+Chl+Cpx+Mag+Ilm,

Figure 10b). Indeed, the assemblage Hgr+Clc+Di is typical of current seafloor rodingites (Frost et al., 2008; Früh-Green, Plas, & Dell'Angelo, 1996). Moreover, these P - T conditions are similar to those estimated by O'Hanley et al. (1992) ($\sim 300^\circ C$, < 800 bar) and Frost et al. (2008) ($\sim 350^\circ C$, 0.4–1 kbar) for modern rodingitization at the seafloor, and with those calculated by Bach and Klein (2009) (200 – $300^\circ C$ at 500 bar) for gabbro rodingitization by fluids related to serpentinization of host peridotites. Furthermore, the amounts of garnet (63–65 wt%), chlorite (18–23 wt%), and clinopyroxene (6–18 wt%) calculated for rodingites formed at $300^\circ C$ (Bach & Klein, 2009; their fig. 10) match our results at 100 – $325^\circ C$ (Figure 10b, green-labelled field): 64–70 wt% garnet, 18–19 wt% chlorite, and 6–8 wt% diopside. Moreover, when the latter data are expressed as vol.% (61–65% garnet, 20–24% chlorite, 6–9.5% diopside), they also match very well the observed modal amounts in Grand-metarodingite (Table 1): 66% garnet, 23% chlorite, 6.5% diopside.

The low $\log fO_2$ calculated for the primitive rodingite assemblage ($\log fO_2 = -55$ to -35 , above FMQ ranging

from +2 to +3, Figure 10b) supports rodingitization occurring simultaneously with serpentinization at very reducing conditions (Charlou, Donval, Fouquet, Jean-Baptiste, & Holm, 2002; Frost & Beard, 2007; Frost, Evans, Swapp, Beard, & Mothersole, 2013; Frost et al., 2008). The composition of Grt-1 ($\text{Gr}_{64-84} \text{Adr}_{5-19} \text{Prp}_{0-1} \text{Alm}_{0-3} \text{Sp}_{80-1} \text{Ti-Gr}_{2-11} \text{Kat}_{1-5}$) is similar to that of hydrogrossular garnet in seafloor rodingites, but with lower katoite amounts (13–16 mol.%; Frost et al., 2008; Rossman & Aines, 1991). This depletion in water probably reflects the progressive dehydration of Grt-1 by Reaction 2 and constitutes the first subduction-related compositional change in garnet after seafloor rodingitization.

Garnet similar to Grt-1 occurs in metarodingites equilibrated at subgreenschist to greenschist facies (Boev, Mircovski, & Korikovski, 1999; Koutsovitis et al., 2013; Mittweide & Schandl, 1992; O'Hanley et al., 1992; Perraki et al., 2010; Pomonis, Tsikouras, Karipi, & Hatzipanagioutou, 2008; Schandl et al., 1989; Tsikouras, Karipi, & Hatzipanagioutou, 2013). It is also preserved in metarodingites that reached eclogite facies conditions (Crossley, Evans, Reddy, & Lester, 2017; Ferrando et al., 2010; Li et al., 2008).

For the Cerro del Almirez metarodingites, complete rodingitization at the seafloor is supported by: (a) the lack of relict igneous protoliths or intermediate assemblages in the inner parts of the bodies; and (b) the widespread occurrence of the rodingitic assemblage (Grt-1+Chl+Cpx+Mag+Ilm) in Grand-metarodingite bodies.

5.2 | Subduction evolution of metarodingites before the antigorite breakdown in host serpentinites

5.2.1 | Type 1 grandite-metarodingite

After rodingitization at the seafloor, mineralogical changes in metarodingites were mainly driven by subduction-related, prograde metamorphic reactions and by interaction with fluids derived from dehydration and redox reactions in the host Atg-serpentinite (Figure 13; stages 2–4). From ~150 to 325°C, depending on pressure, the early assemblage Grt-1+Chl+Cpx+Mag+Ilm was stable at log $f\text{O}_2$ conditions corresponding to the FMQ-buffer and andradite contents progressively increased in garnet (Figure 10b). The maximum pressure of stability of Grt-1 cannot be precisely constrained but must be lower than 10 kbar, as supported by the higher amounts of pyralspite components calculated at this pressure (5–10 mol.%, blue isopleths in Figure 10c) compared to those in Grt-1 (<3 mol.% pyralspite).

In the first set of veins that cut Grand-metarodingites, scarce garnet grains occur (Grt-2a; Figure 6a,b) with high

andradite (24–20 mol.%) and low pyralspite (3–4 mol.%; green dots in Figure 5). The thermodynamic model predicts that similar andradite-rich compositions are stable at >300°C and log $f\text{O}_2 = -30$ to -23 , inbetween that of FMQ and MH (Figure 10b) and coexist with phases (epidote and spinel) that are not observed in Grand-metarodingite. We thus suggest that Grt-2a crystallized during an episodic flux of oxidizing fluids that were not buffered by the metarodingite mineral assemblage. Therefore, Grt-2a was not in equilibrium with the bulk-rock composition and cannot be reproduced by thermodynamic models. Such oxidizing fluids may have been released by the transformation of lizardite to antigorite, concomitant with a decrease in the magnetite modal amount, at 300–325°C (Debret et al., 2015) in host serpentinites. This process has been reported in several Alpine serpentinite localities (Debret et al., 2014) and might be the reason for the ubiquitous formation of garnet similar to Grt-2a in low to medium grade metarodingite outcrops (Dubinska, 1995; Hatzipanagioutou & Tsikouras, 2001; Koutsovitis et al., 2013; Mittweide & Schandl, 1992).

Grt-2b is the main component of the first vein generation (Figure 6a,b) and also occurs in chlorite-rich and diopside-poor domains of the matrix or as thin rims surrounding Grt-1. Grt-2b is calculated to be stable with chlorite and titanite at significantly higher temperature (560–675°C) and pressure conditions (9–20 kbar) than Grt-1 (Figure 10a). However, at oxygen fugacity above FMQ buffer, this assemblage can be stable at temperatures as low as 350°C (Figure 10c).

The change from the assemblage Grt-1+Chl+Cpx+Mag+Ilm to the assemblage Grt-2b+Chl+Ttn reflects the simultaneous development of a set of prograde metamorphic reactions in Grand-metarodingites: Grt-1 partially broke down and dehydrated (Reaction 2), reacted with magnetite (that almost disappeared) producing the almandine and andradite components of Grt-2b (Reaction 3) and released Ti from the morimotoite component producing significant amounts of titanite (Reaction 5). Reactions 1 and 5 consumed diopside and may thus explain its lack in the Grt-2b-bearing domains of Grand-metarodingites.

The Grt-2b+Chl+Ttn assemblage was stable at higher log $f\text{O}_2$ conditions (between the FMQ and MH buffers) compared to Grt-1-bearing assemblages, probably owing to the release of water by Reaction 2 (Figure 10c). In this diagram, vesuvianite is expected to be stable at buffered FMQ conditions and temperatures above 550°C. This might explain the presence of this phase in other metarodingites equilibrated at high temperature and pressure (e.g., Li et al., 2004, 2008; Zaroni et al., 2016). In the case of metarodingites from Cerro del Almirez, log $f\text{O}_2$ remained buffered at higher values by the rock mineral assemblage, as evidenced by the parallel orientation of the assemblage stability fields to the oxygen buffers (Figure 10c).

Granditic garnet with significant pyralspite contents, as is the case of Grt-2b (up to 16 mol.%), has been reported in other high- P metarodingites (Evans et al., 1979; Ferrando et al., 2010; their Type II and Type IV veins; Crossley et al., 2017). Isopleths from Figure 10a demonstrate that the amount of the garnet pyralspite component in the metarodingite system increases with pressure and temperature, allowing the stability conditions of the Grt-2b-bearing assemblage to be constrained.

Grt-3 is the main component of the second vein generation and also rims previous garnet (Figure 6a,b). The Grt-3 composition cannot be reproduced in the P - T pseudosection from Figure 10a suggesting that it was not buffered by the mineral assemblage, but from external fluids that induced changes in oxygen fugacity. However, T - $\log fO_2$ calculations are not precise enough in constraining the conditions of Grt-3 formation (Figure 10c). As textural relationships indicate that Grt-3 formed after Grt-2b, the minimum pressure of its stabilization can be fixed at 10 kbar. Considering the garnet isopleths and the limiting stability of rutile, the temperature of Grt-3 crystallization was $>525^\circ\text{C}$ at $\log fO_2 > -19$, over and above that of MH (Figure 10c, yellow-labelled fields). At these conditions, the thermodynamic model predicts the presence of small amounts of coexisting epidote that are also observed in some veins.

High fO_2 conditions during the formation of Grt-3 were possibly induced by the release of oxidizing fluids due to magnetite destabilization during brucite breakdown in host serpentinite or even during the progressive decrease in the antigorite amount in serpentinites between 550 and 650°C, at 20 kbar, as observed in experimental determinations (Merkulova, Muñoz, Vidal, & Brunet, 2016; Merkulova et al., 2017). In the Cerro del Almirez Atg-serpentinites, brucite breakdown occurred at 10 kbar and $\sim 475^\circ\text{C}$ (López-Sánchez-Vizcaíno et al., 2005, 2009; Padrón-Navarta et al., 2012). Accordingly, Grt-3 veins might have formed in a wide temperature range between ~ 475 and 625°C in Grand-metarodingite (Figure 13; stage 4). Discrepancy with the mineral assemblages in Figure 10c can be explained by the lack of complete thermodynamic equilibrium between the metarodingite mineral assemblages and the external oxidizing fluids that fluxed through them.

Andradite-rich garnet similar to Grt-3 was reported by Li et al. (2004, 2008) and Ferrando et al. (2010; their veins V). In the former case, a distinct and continuous change in fO_2 is invoked that progressed from ocean-floor metamorphism to initial burial and then subduction (Li et al., 2004).

Thin veinlets with Grt-2b composition cut Grt-3 veins (white stars in Figure 6a,b) and they may record the stop in the percolation of oxidizing fluids and the restoration of fO_2 conditions buffered by the rock mineral assemblage. Alternation of andradite-rich (equivalent to our Grt-3) and

andradite-poor (equivalent to our Grt-2b) garnet generations was also described by Ferrando et al. (2010), but they did not explore the potential reasons for it.

Grt-3 with the highest andradite contents (up to 53 mol.%) is also in equilibrium within Ep-metarodingites close to the Atg-serpentinite dehydration front. This indicates that oxidizing conditions finally stabilized at $\log fO_2 > -20$, over and above that of MH (Figure 11b) at P - T conditions close to those of Atg breakdown ($\sim 650^\circ\text{C}$ and 16–19 kbar, Padrón-Navarta et al., 2012).

5.2.2 | Grandite- to epidote-metarodingite transformation

The formation of Ep-metarodingite after Grand-metarodingite at Cerro del Almirez was the result of the growth of epidote after the hydration (Reaction 6) and oxidation (Reaction 7) of grandite garnet and of the growth of diopside after chlorite breakdown (Reaction 8). This partial or total transformation was driven by the increase of μSiO_2 and the drop of μCaO at H_2O -saturated and high fO_2 conditions (Figure 11a). The gradients of chemical potentials during metamorphism were controlled by the strong compositional differences between the CaO-rich Grand-metarodingites and their MgO- and SiO_2 -richer host rocks, including the diopside-bearing metasomatic rims. The extent of transformation of Grand-metarodingite bodies within the Atg-serpentinite domain is very variable. In most cases, transformation was only incipient (Figure 2a). At the thin section scale, millimetre to centimetre square-sized domains can be found that display the complete transition between the garnet-bearing assemblages and those consisting of epidote–diopside–titanite and minor amounts of Grt-3 (Figure S2), as reproduced by the path (white arrow) in the calculated pseudosection from Figure 11a.

Transformation to homogeneous Ep-metarodingite is well developed only in some boudins close to the dehydration front (Figure 2d), thus indicating that, in this region, the physicochemical conditions were more favourable to the change. In this case, mineral modes indicate that Reactions 6–8 completely consumed garnet and chlorite. During garnet destabilization, mobile components CaO and SiO_2 were released by Reaction 6 and consumed by Reaction 7. However, grandite components (involved in Reaction 6) in Grt-1, -2b, and -3 were much more abundant than almandine (involved in Reaction 7) and, thus, the global balance of garnet breakdown resulted in the release of CaO and SiO_2 . Due to the higher abundance of garnet compared to chlorite in Grand-metarodingite (66 and 23 vol.%, respectively), the amount of these two mobile components contributed to the simultaneous chlorite destabilization through the CaO- (19 moles per 3 moles of consumed chlorite) and, especially, SiO_2 -consuming (27 moles per 3 moles of

chlorite; Reaction 8). The net balance of Grand- to Ep-metaroddingite transformation was CaO liberation and SiO₂ absorption (Figures 8a and 11a). Released CaO most probably diffused towards the borders of the metaroddingite bodies and contributed to the growth of Chl-Di- and Chl-Di-Ol-metasomatic rims. These reaction rims are clearly thicker in the boudins with well-developed Ep-metaroddingite zones (Figure 2b) than around poorly transformed Grand-metaroddingites (Figure 2a). On the contrary, silica consumed during the formation of Ep-metaroddingite likely diffused from the SiO₂-rich wall rocks to the metaroddingite bodies.

Element diffusion and chemical potential gradients are clearly enhanced by the presence of a free fluid in the rocks (e.g., Gasc et al., 2016). However, water amounts released by chlorite breakdown through Reaction 8 were not sufficient for inducing fluid saturation required by the thermodynamic model (Figure 11), as evidenced by the preservation of grandite garnet in rock domains in which chlorite has already been transformed to diopside (Figure S2). Thus, an additional external fluid released from host Atg-serpentinite must be invoked to favour element diffusion in metaroddingites. The higher abundance of Ep-metaroddingite close to the dehydration front is in agreement with a higher concentration of fluids in these areas.

Two possible mechanisms of fluid production in serpentinites that did not reach the conditions of antigorite breakdown (~16–19 kbar, 650°C) are the OH-titanian clinohumite breakdown reaction (López-Sánchez-Vizcaíno et al., 2005, 2009; and references therein) and the antigorite consuming diopside-out, tremolite-in reaction (Trommsdorff & Evans, 1974). Considering the very low abundance of Ti-Chu compared to antigorite and diopside, the latter reaction was much more relevant in the Cerro del Almiraz serpentinite (Jabaloy-Sánchez et al., 2015; López-Sánchez-Vizcaíno et al., 2009). Both reactions, nevertheless, were almost simultaneous at well-known pressure and temperature ranges (16–19 kbar and 620–630°C; López-Sánchez-Vizcaíno et al., 2009; Padrón-Navarta et al., 2012), thus constraining the onset of transformation of Grand-metaroddingite into Ep-metaroddingite at these conditions (Figure 13; stage 5). Experimental determinations by Merkulova et al. (2017) also agree with a progressive decrease in the antigorite amount in serpentinites between 550 and 650°C at 20 kbar accompanied by a progressive loss of H₂O.

The irregular distribution of Ep-metaroddingites in the Atg-serpentinite domain and their higher abundance close to the dehydration front attest to a very irregular flux pattern of fluids within metaroddingites. Even in the case of the most transformed boudins, the distribution of Ep-metaroddingite lacks a well-defined development pattern (e.g., from rims to core) suggesting that the transformation into

Ep-metaroddingite progressed only in the boudin volume that attained fluid saturation.

The calculated prevailing oxidized conditions for the formation of Ep-metaroddingites (Figure 11b) and their generally higher Fe³⁺/Fe_{Total} compared to Grand-metaroddingites (Figure 8b) might be due to the combined effects of oxidizing Reaction 7 and oxidizing external fluids that fluxed through metaroddingites. Calculations of Debret and Sverjensky (2017) point to high oxygen fugacity and high amounts of dissolved sulphates in fluids released from dehydrating serpentinites at the onset of tremolite formation and magnetite consumption (>630°C, 20 kbar). Oxygen release during progressive and simultaneous breakdown of antigorite and magnetite at similar *P–T* conditions was also reported in experiments (Merkulova et al., 2017). Formation of Ep-metaroddingites from the Atg-serpentinite domain at oxidizing conditions also accounts for the composition of Grt-3 in these rocks, which has the highest andradite contents of any garnet type in the Cerro del Almiraz metaroddingites (dark yellow triangles in Figure 5).

5.3 | Evolution of metaroddingites during and after serpentinite dehydration

5.3.1 | Type 2 epidote-metaroddingite

Beyond the dehydration front, that is, within the Chl-harzburgite domain, all the metaroddingite bodies are transformed into Ep-metaroddingite, and Grand-metaroddingite only occurs as scarce relicts in the core of some boudins. This supports the hypothesis that flux of high amounts (~9 wt% H₂O; Padrón-Navarta, Tommasi, et al., 2010) of oxidizing fluids (Debret & Sverjensky, 2017; Debret et al., 2015; Merkulova et al., 2017) released during Atg-breakdown in serpentinite favored the transformation of Grand-metaroddingite into Ep-metaroddingite (Figure 13, stage 6).

However, Ep-metaroddingites in the Atg-serpentinite and Chl-harzburgite domains show significant mineralogical and compositional differences, in particular the presence in the latter of (a) a new generation of progressively pyralspite-richer garnet (Grt-4; Figure 5) in equilibrium with epidote–diopside–titanite and (b) a generally lower bulk Fe³⁺/Fe_{Total} ratio (Figure 8b). Grt-4 formed by re-equilibrium of relict Grt-2b and Grt-3 grains, as evidenced by their higher pyralspite contents, which increase towards the borders, and the common precipitation of idiomorphic rims. H₂O saturation conditions and increasing temperatures facilitated this re-equilibrium (Ague & Carlson, 2013) as well as the large reactive surface of the grains owing to their small size and irregular shape. Equilibrium conditions of Grt-4 have been calculated at 16 kbar, 670°C, log *f*O₂ = –14.5 and H₂O-saturated conditions (yellow star in Figure 11b), well within the stability field of Chl-harzburgite.

This log fO_2 value matches the estimations of Debret et al. (2015) for the host Chl-harzburgite.

Due to the strong compositional differences between metarodingites and their host ultramafic rocks, chemical potential gradients of CaO and MgO were the driving forces of the change of Grt-4 composition towards pyral-spite-rich contents (as indicated by the values of garnet isopleths along the white arrow in Figure 12a). The direction of the μMgO gradient was opposite to that of μCaO (Figure 13, stage 6) and was probably responsible for the observed stabilization of chlorite richer zones around metarodingite boudins (Li et al., 2004), but this effect was not evident in their cores. This only happened when the boudins were small enough, as is the case of the Ep-metarodingites hosted by Chl-harzburgite.

5.3.2 | Ep- to Pyral-metarodingite transformation

With increasing temperature, retention of the μCaO and μMgO gradients at H_2O saturation conditions favoured the transformation of Ep-metarodingite into Type 3 Pyral-metarodingite (blue fields in Figure 12a) in some small boudins of the Chl-harzburgite domain (Figure 2f).

This transformation occurred through epidote-consuming Reactions 10 and 11, which, respectively, account for the pyrope and almandine components in the crystallization of Grt-5. However, Reaction 11 is a reducing reaction. The driving force of this reduction might have been the strong gradient in the oxygen quantity (nO_2 ; Evans, 2006; Tumiati, Godard, Martin, Malaspina, & Poli, 2015) between Ep-metarodingite and host Chl-harzburgites, as revealed by the sharp difference in their Fe^{3+}/Fe_{Total} ratios: ~ 0.8 and $0.25\text{--}0.5$ respectively (Figure 8b). These low values in Chl-harzburgite can be explained by the strong drop in Fe^{3+}/Fe_{Total} ratio produced during the transformation of Atg-serpentinite ($0.63\text{--}0.74$) into Chl-harzburgite owing to the very significant reduction of Fe^{3+} hosted in both magnetite and antigorite during dehydration (Debret et al., 2015). The subsequent transformation of Ep-metarodingite into Pyral-metarodingite caused the progressive change of the Fe^{3+}/Fe_{Total} ratio in metarodingites, which finally re-equilibrated at values ($0.38\text{--}0.35$) within the range of Chl-harzburgites (Figure 8b). Increasing μMgO and decreasing μCaO (Figure 12a) also triggered the crystallization of tremolitic amphibole (Amp-1) in Pyral-metarodingite by diopside-consuming Reaction 12.

Despite significant changes in μMgO , μCaO and Fe^{3+}/Fe_{Total} , thermodynamic equilibrium was reached in Pyral-metarodingite as evidenced by the good agreement between the modelled stable assemblages, modal amounts and mineral chemistry (Figure 12b) and those observed in rocks. The estimated $P\text{--}T$ conditions calculated for the almandine-

rich cores of Grt-5 (11–16 kbar, 640–650°C), and especially their pyrope-rich rims (15.5–18.5 kbar, 660–684°C; Figure 12b), mark the peak metamorphic conditions of metarodingites. The latter compare very well with independent $P\text{--}T$ determinations for host Chl-harzburgites (16–19 kbar, $<710^\circ C$, López-Sánchez-Vizcaíno et al., 2005, 2009; Padrón-Navarta, Hermann, et al., 2010) and for some ophicarbonates lenses hosted within these same rocks (18 kbar, 650–670°C; Menzel, Garrido, López-Sánchez-Vizcaíno, Marchesi, & Hidas, 2017).

Metarodingites from Cima di Gagnone in the Central Alps are also hosted in Chl-harzburgite formed after serpentinite dehydration (Evans & Trommsdorff, 1978). Similar to the Cerro del Almirez Pyral-metarodingites, they are rich in epidote (up to 25 vol.%), in garnet with composition close to that of Grt-5 and have very similar bulk compositions except for lower Al_2O_3 (Evans, Trommsdorff, & Goles, 1981). All these features support a comparable, subduction-related metamorphic evolution for these two metarodingite suites.

The only previous study of the Cerro del Almirez metarodingites (Puga et al., 1999) used a completely different terminology that is not sustained by our study. According to these authors, only the here-called Grand-metarodingites can be considered as pure metarodingites and all other types are referred to as “eclorodingites,” that is, rocks with “transitional parageneses from rodingites to eclogites,” attributed to metamorphism of protoliths, which underwent different degrees of oceanic metasomatism and Na_2O loss. As discussed, all our results support a very different interpretation: (a) complete seafloor rodingitization affected the mafic protoliths of the Cerro del Almirez metarodingites (Section 5.1); (b) all their mineralogical and bulk compositional changes took place during subduction metamorphism; and (c) all Na_2O present in some rocks was clearly gained during retrograde amphibolitization (see below).

5.3.3 | Retrograde amphibolitization

The mineral assemblages of all metarodingite types from Cerro del Almirez were partially replaced by late Na-bearing Ca-amphibole corresponding to the above-defined Amp-2 (Figures 2e,f and 7). Textural relationships and low bulk Na_2O contents of Grand-metarodingites (Table 3) indicate that amphibolitization was caused by percolation of external alkali-rich fluids. The very low abundances of Na_2O and K_2O in both Atg-serpentinite and Chl-harzburgite (Garrido et al., 2005) support that these fluids were probably released from metasedimentary rocks that host the Cerro del Almirez ultramafic complex (Figure 1a). According to Jabaloy-Sánchez et al. (2015), the Cerro del Almirez ultramafic massif and their host metasedimentary rocks were coupled after the peak of metamorphism and

underwent a common tectonometamorphic evolution during exhumation. The retrograde origin of amphibolitization is also in agreement with textural relationships in Pyrrals-metarodngites, in which Amp-2 crystallization occurred after that of Amp-1, which in turn marks the peak metamorphic conditions in equilibrium with Grt-5.

5.4 | The role of metarodngites in the redox state of subduction zones

Serpentinites and metarodngites are coupled in exhumed metamorphic terranes owing to their simultaneous formation and paired evolution during subduction. Nevertheless, the significance of metarodngites for the petrological and geochemical processes that take place in subduction zones has been usually disregarded. Increasing attention has been recently devoted to the presence of relatively oxidized materials in subduction zones and their role on deep element cycling (e.g., Evans & Powell, 2015; Malaspina et al., 2017; Tumiati et al., 2015). Oxidizing agents may be transported into the subarc mantle by metamorphic fluids produced by devolatilization of the subducting slab (Evans, 2012). The oxidizing capacity of these fluids relative to a reference state (the redox budget; Evans, 2006) is of great importance for the composition of arc magmatism and arc-related ore deposits (Evans & Powell, 2015 and references therein). The role of dehydration reactions in serpentinite for the redox state of subduction zones has been well studied (Debret & Sverjensky, 2017; Debret et al., 2014, 2015; Merkulova et al., 2017). These studies emphasized the importance of fluids released from serpentinites as oxidizing agents of adjacent slab lithologies (mostly anhydrous mantle peridotites) at the metre scale. However, metarodngites have been rarely considered in the studies of fluid–rock interactions in subduction zones (Crossley et al., 2017).

The metarodngites from the Cerro del Almirez ultramafic complex are an illustrative and unique case study of the subduction evolution of igneous mafic rocks originally rodingitized at the seafloor. Their mineralogical, textural, and compositional features, generally reproduced by the thermodynamic models presented in this work (Figures 10–12), reveal that metarodngites were affected by the main dehydration and redox reactions that occurred in their host serpentinite.

Higher Fe^{3+}/Fe_{Total} ratios in Ep- than in Grand-metarodngites (Figure 8b) indicate that metarodngites oxidized during dehydration of host serpentinites up to Atg-breakdown. Thus, metarodngite bodies enclosed in Atg-serpentinites, and in their reaction product Chl-harzburgites, acted as sinks of oxidizing fluids travelling from dehydrating serpentinites to the inner mantle wedge. Subsequent transformation into Pyrrals-metarodngite strongly decreased Fe^{3+}/Fe_{Total} , which reached values in equilibrium with the host Chl-

harzburgite (Figure 8b). Therefore, the transformation of Ep-metarodngite into Pyrrals-metarodngite further released oxidizing fluids at temperatures $\sim 40^{\circ}C$ higher than those corresponding to Atg-breakdown (Figure 13; stage 7).

However, field observations in Cerro del Almirez show that Type 3 Pyrrals-metarodngites are scarce, and so significant volumes of Fe^{3+} -rich metarodngite boudins (Type 1 and Type 2) were metastably preserved within the Chl-harzburgite domain far beyond the antigorite dehydration front (Figure 1b). The kinetic limitation for reequilibration can be explained by the strong rheology (dominated by garnet, e.g., Karato, Wang, Liu, & Fujino, 1995) and the intrinsically low permeability (e.g., Katayama, Terada, Okazaki, & Tanikawa, 2012) of metarodngites. Similar preservation of metastable metarodngite bodies is reported also at Cima di Gagnone (Evans et al., 1979). This suggests that Fe^{3+} -rich, metastable metarodngites can be transported to the deep mantle through subduction, and their recycling into the asthenosphere may affect the oxidation state of the deep Earth.

6 | CONCLUSIONS

Field and textural relationships, mineral and bulk-rock compositions, chemographic analyses, and thermodynamic models constrain the subduction evolution of metarodngites from Cerro del Almirez, the unique locality in the world where the Atg-out isograd in subducted serpentinite has been recognized in the field. After complete rodingitization of igneous mafic protoliths at highly reducing conditions in a seafloor setting (<2 kbar, ~ 150 – $325^{\circ}C$, $\sim FMQ$ buffer), Grand-metarodngite (grossular-rich garnet (Grt-1), diopside, chlorite, and magnetite) recrystallized during subduction. Then, two generations of garnet formed in Grand-metarodngite by prograde metamorphism at high pressure (>10 kbar, ~ 350 – $650^{\circ}C$). Grt-2b, which is richer in andradite and pyrralspite components than Grt-1, crystallized at conditions buffered by the metarodngite bulk-rock compositions (fO_2 – FMQ buffer). Grt-3, notably richer in andradite, formed during flux of oxidizing fluids likely released from brucite and antigorite breakdown in host Atg-serpentinites (fO_2 – MH buffer). Transformation of Grand-metarodngite into Ep-metarodngite (epidote, diopside, garnet, and titanite), was driven by the simultaneous effects of increasing μSiO_2 and decreasing μCaO gradients, triggered by the flux of high amounts of oxidizing fluids released during high-pressure final Atg-breakdown in host serpentinites. Within Chl-harzburgites produced by serpentinite dehydration, some epidote-metarodngite bodies transformed into pyrralspite-metarodngites (Grt-5, tremolitic Amp-1, epidote, zoisite, chlorite and rutile) at peak metamorphic conditions (16–19 kbar, 660 – $684^{\circ}C$) by

decreasing μCaO and increasing μMgO gradients and inducing a strong drop in the bulk-rock $\text{Fe}^{3+}/\text{Fe}_{\text{Total}}$ ratio. The contrasting $\text{Fe}^{3+}/\text{Fe}_{\text{Total}}$ ratios between Atg-serpentinite and Chl-harzburgite, and between the three metaroddingite types enclosed in these ultramafic rocks attest for the highly heterogeneous oxidation degree of the subducting slab and the role of metaroddingites in the transfer of oxidized materials to the deep mantle beyond the Atg-out isograd in subducted serpentinites.

ACKNOWLEDGMENTS

We thank two anonymous referees and the editor for their constructive reviews of the manuscript. We acknowledge M. J. Román-Alpiste for his help in sample analysis and preparation. The Sierra Nevada National Park is also acknowledged for providing permits for fieldwork and sampling. Research leading to these results was funded by C.L.L.'s Ph.D. project BES-2013-065336, by grants no. CGL2012-32067 and CGL2016-75224-R from the Spanish "Ministerio de Economía, Industria y Competitividad" (MINECO) and "Junta de Andalucía" research group RNM-145 and grant P12-RNM-3141. C.M. acknowledges funding by Ramón y Cajal fellowship RYC-2012-11314 and grant no. CGL2016-81085-R from MINECO and "Junta de Andalucía" research group RNM-131. C.J.G. acknowledges funding from MINECO grant no. PCIN-2015-053. Research grants, infrastructures and human resources leading to this research have benefited from funding by European Social Fund and the European Regional Development Fund. This work received (co)-funding from the European Social Fund and the European Regional Development Fund.

ORCID

Casto Laborda-López  <http://orcid.org/0000-0002-2172-5997>

REFERENCES

- Ague, J. J., & Carlson, W. D. (2013). Metamorphism as garnet sees it: The kinetics of nucleation and growth, equilibration, and diffusional relaxation. *Elements*, 9(6), 439–445. <https://doi.org/10.2113/gselements.9.6.439>
- Alt, J. C., Garrido, C. J., Shanks, W. C., Turchyn, A., Padrón-Navarta, J. A., López-Sánchez-Vizcaíno, V., ... Marchesi, C. (2012). Recycling of water, carbon, and sulfur during subduction of serpentinites: A stable isotope study of Cerro del Almirez, Spain. *Earth and Planetary Science Letters*, 327, 50–60. <https://doi.org/10.1016/j.epsl.2012.01.029>
- Andersen, D. J., & Lindsley, D. H. (1988). Internally consistent solution models for Fe-Mg-Mn-Ti oxides: Fe-Ti oxides. *The American Mineralogist*, 73(7–8), 714–726.
- Andrut, M., Wildner, M., & Beran, A. (2002). The crystal chemistry of birefringent natural uvarovites. Part IV. OH defect incorporation mechanisms in non-cubic garnets derived from polarized IR spectroscopy. *European Journal of Mineralogy*, 14(6), 1019–1026. <https://doi.org/10.1127/0935-1221/2002/0014-1019>
- Anhaeusser, C. R. (1979). Roddingite occurrences in some Archaean ultramafic complexes in the Barberton Mountain Land, South-Africa. *Precambrian Research*, 8(1–2), 49–76. [https://doi.org/10.1016/0301-9268\(79\)90038-X](https://doi.org/10.1016/0301-9268(79)90038-X)
- Antao, S. M., Zaman, M., Gontijo, V. L., Camargo, E. S., & Marr, R. A. (2015). Optical anisotropy, zoning, and coexistence of two cubic phases in andradites from Quebec and New York. *Contributions to Mineralogy and Petrology*, 169(2), 10. <https://doi.org/10.1007/s00410-015-1104-0>
- Arshinov, V. V., & Merenkov, B. (1930). Petrology of the chrysotile asbestos deposits of the Krasnouralky Mine in the Ural Mountains. *Transactions of the Institute of Economic Mineralogy and Metallurgy*, 45, 1–83.
- Attoh, K., Evans, M. J., & Bickford, M. E. (2006). Geochemistry of an ultramafic-rodingite rock association in the Paleoproterozoic Dixcove greenstone belt, southwestern Ghana. *Journal of African Earth Sciences*, 45(3), 333–346. <https://doi.org/10.1016/j.jafrearsci.2006.03.010>
- Aumento, F., & Loubat, H. (1971). The Mid-Atlantic ridge near 45° N. XVI. Serpentinized ultramafic intrusions. *Canadian Journal of Earth Sciences*, 8(6), 631–663. <https://doi.org/10.1139/e71-062>
- Austrheim, H., & Prestvik, T. (2008). Roddingitization and hydration of the oceanic lithosphere as developed in the Leka ophiolite, north-central Norway. *Lithos*, 104(1–4), 177–198. <https://doi.org/10.1016/j.lithos.2007.12.006>
- Bach, W., & Klein, F. (2009). The petrology of seafloor rodingites: Insights from geochemical reaction path modeling. *Lithos*, 112(1–2), 103–117. <https://doi.org/10.1016/j.lithos.2008.10.022>
- Bakker, H. E., Jong, K. D., Helmers, H., & Biermann, C. (1989). The geodynamic evolution of the Internal Zone of the Betic Cordilleras (south-east Spain): A model based on structural analysis and geothermobarometry. *Journal of Metamorphic Geology*, 7(3), 359–381. <https://doi.org/10.1111/j.1525-1314.1989.tb00603.x>
- Banno, S. (1986). The high-pressure metamorphic belts of Japan: A review. *Geological Society of America Memoir*, 164, 365–374. <https://doi.org/10.1130/MEM164>
- Barnicoat, A. C., & Fry, N. (1986). High-pressure metamorphism of the Zermatt-Saas ophiolite zone, Switzerland. *Journal of the Geological Society*, 143(4), 607–618. <https://doi.org/10.1144/gsjgs.143.4.607>
- Beard, J. S., Fullagar, P. D., & Krishna Sinha, A. (2002). Gabbroic pegmatite intrusions, Iberia Abyssal Plain, ODP Leg 173, Site 1070: Magmatism during a transition from non-volcanic rifting to sea-floor spreading. *Journal of Petrology*, 43(5), 885–905. <https://doi.org/10.1093/petrology/43.5.885>
- Behr, W. M., & Platt, J. P. (2012). Kinematic and thermal evolution during two-stage exhumation of a Mediterranean subduction complex. *Tectonics*, 31(4).
- Bell, J. M., Clarke, E. C., & Marshall, P. (1911). The geology of the Dun Mountain subdivision, Nelson. New Zealand Geological Survey Bulletin 12 new series. Mackay, government printer.
- Benson, W. N. (1913). The geology and petrology of the Great Serpentine belt of New South Wales. Part 1. Introduction, *Proceedings of the Linnean Society of N.S.W.*, 38, 491–517.

- Berger, A., & Bousquet, R. (2008). Subduction-related metamorphism in the Alps: Review of isotopic ages based on petrology and their geodynamic consequences. *Geological Society, London, Special Publications*, 298(1), 117–144. <https://doi.org/10.1144/SP298.7>
- Boev, B., Mircovski, V., & Korikovski, S. (1999). Rodingite rocs in the Jurassic serpentinite masses from the area of Rzanovo, Republic of Macedonia. *Geologica Macedonica*, 13, 75–84.
- Booth-Rea, G., Ranero, C. R., Martínez-Martínez, J. M., & Grevermeyer, I. (2007). Crustal types and Tertiary tectonic evolution of the Alborán sea, western Mediterranean. *Geochemistry, Geophysics, Geosystems*, 8(10), Q10005. <https://doi.org/10.1029/2007GC001639>
- Cannò, E., Agostini, S., Scambelluri, M., Tonarini, S., & Godard, M. (2015). B, Sr and Pb isotope geochemistry of high-pressure Alpine metaperidotites monitors fluid-mediated element recycling during serpentinite dehydration in subduction mélange (Cima di Gagnone, Swiss Central Alps). *Geochimica et Cosmochimica Acta*, 163, 80–100. <https://doi.org/10.1016/j.gca.2015.04.024>
- Charlou, J. L., Donval, J. P., Fouquet, Y., Jean-Baptiste, P., & Holm, N. (2002). Geochemistry of high H₂ and CH₄ vent fluids issuing from ultramafic rocks at the Rainbow hydrothermal field (36°14' N, MAR). *Chemical Geology*, 191(4), 345–359. [https://doi.org/10.1016/S0009-2541\(02\)00134-1](https://doi.org/10.1016/S0009-2541(02)00134-1)
- Coleman, R. G. (1963). Serpentinities, rodingites, and tectonic inclusions in Alpine-type mountain chains. *Geological Society of America Special Papers*, 73, 130–131.
- Coleman, R. G. (1967). Low-temperature reaction zones and alpine ultramafic rocks of California, Oregon, and Washington. *United States Geological Survey Bulletin*, 1247, 1–49.
- Cronnelly, J. (2009). The geodynamic equation of state: What and how. *Geochemistry, Geophysics, Geosystems*, 10(10).
- Crossley, R. J., Evans, K. A., Reddy, S. M., & Lester, G. W. (2017). Redistribution of iron and titanium in high-pressure ultramafic rocks. *Geochemistry, Geophysics, Geosystems*, 18(11), 3869–3890. <https://doi.org/10.1002/2017GC007145>
- Dale, J., Holland, T., & Powell, R. (2000). Hornblende-garnet-plagioclase thermobarometry: A natural assemblage calibration of the thermodynamics of hornblende. *Contributions to Mineralogy and Petrology*, 140(3), 353–362. <https://doi.org/10.1007/s004100000187>
- Debret, B., Andreani, M., Muñoz, M., Bolfan-Casanova, N., Carlut, J., Nicollet, C., ... Trcera, N. (2014). Evolution of Fe redox state in serpentine during subduction. *Earth and Planetary Science Letters*, 400, 206–218. <https://doi.org/10.1016/j.epsl.2014.05.038>
- Debret, B., Bolfan-Casanova, N., Padrón-Navarta, J. A., Martín-Hernández, F., Andreani, M., Garrido, C. J., ... Trcera, N. (2015). Redox state of iron during high-pressure serpentinite dehydration. *Contributions to Mineralogy and Petrology*, 169(4), 36. <https://doi.org/10.1007/s00410-015-1130-y>
- Debret, B., & Sverjensky, D. A. (2017). Highly oxidising fluids generated during serpentinite breakdown in subduction zones. *Scientific Reports*, 7(1), 10351. <https://doi.org/10.1038/s41598-017-09626-y>
- Dubinska, E. (1995). Rodingites of the eastern part of the Jordanow-Gogolow serpentinite massif, Lower Silesia, Poland. *The Canadian Mineralogist*, 33(3), 585–608.
- Ernst, W. (2011). Accretion of the Franciscan Complex attending Jurassic-Cretaceous geotectonic development of northern and central California. *Geological Society of America Bulletin*, 123(9–10), 1667–1678. <https://doi.org/10.1130/B30398.1>
- Evans, B. W. (2004). The serpentinite multisystem revisited: Chrysotile is metastable. *International Geology Review*, 46(6), 479–506. <https://doi.org/10.2747/0020-6814.46.6.479>
- Evans, K. A. (2006). Redox decoupling and redox budgets: Conceptual tools for the study of earth systems. *Geology*, 34(6), 489–492. <https://doi.org/10.1130/G22390.1>
- Evans, K. A. (2012). The redox budget of subduction zones. *Earth-Science Reviews*, 113(1–2), 11–32. <https://doi.org/10.1016/j.earscirev.2012.03.003>
- Evans, K. A., & Powell, R. (2015). The effect of subduction on the sulphur, carbon and redox budget of lithospheric mantle. *Journal of Metamorphic Geology*, 33(6), 649–670. <https://doi.org/10.1111/jmg.12140>
- Evans, B. W., & Trommsdorff, V. (1978). Petrogenesis of garnet lherzolite, Cima di Gagnone, Lepontine Alps. *Earth and Planetary Science Letters*, 40(3), 333–348. [https://doi.org/10.1016/0012-821X\(78\)90158-9](https://doi.org/10.1016/0012-821X(78)90158-9)
- Evans, B. W., Trommsdorff, V., & Goles, G. G. (1981). Geochemistry of high-grade eclogites and metarodingites from the Central Alps. *Contributions to Mineralogy and Petrology*, 76(3), 301–311. <https://doi.org/10.1007/BF00375457>
- Evans, B. W., Trommsdorff, V., & Richter, W. (1979). Petrology of an eclogite-metarodingite suite at Cima di Gagnone, Ticino, Switzerland. *American Mineralogist*, 64(1–2), 15–31.
- Ferrando, S., Frezzotti, M. L., Orione, P., Conte, R. C., & Compagnoni, R. (2010). Late-Alpine rodingitization in the Bellecombe meta-ophiolites (Aosta Valley, Italian Western Alps): Evidence from mineral assemblages and serpentinization-derived H₂-bearing brine. *International Geology Review*, 52(10–12), 1220–1243. <https://doi.org/10.1080/00206810903557761>
- Frost, B. R. (1975). Contact metamorphism of serpentinite, chloritic blackwall and rodingite at Paddy-Go-Easy Pass, Central Cascades, Washington. *Journal of Petrology*, 16(2), 272–313. <https://doi.org/10.1093/petrology/16.1.272>
- Frost, B. R., & Beard, J. S. (2007). On silica activity and serpentinization. *Journal of Petrology*, 48(7), 1351–1368. <https://doi.org/10.1093/petrology/egm021>
- Frost, B. R., Beard, J. S., McCaig, A., & Condliffe, E. (2008). The formation of micro-rodingites from IODP Hole U1309D: Key to understanding the process of serpentinization. *Journal of Petrology*, 49(9), 1579–1588. <https://doi.org/10.1093/petrology/egn038>
- Frost, B. R., Evans, K. A., Swapp, S. M., Beard, J. S., & Mothersole, F. E. (2013). The process of serpentinization in dunite from New Caledonia. *Lithos*, 178, 24–39. <https://doi.org/10.1016/j.lithos.2013.02.002>
- Früh-Green, G. L., Kelley, D. S., Bemasoni, S. M., Karson, J. A., Ludwig, K. A., Butterfield, D. A., ... Proskurowski, G. (2003). 30,000 years of hydrothermal activity at the Lost City vent field. *Science*, 301(5632), 495–498. <https://doi.org/10.1126/science.1085582>
- Früh-Green, G. L., Orcutt, B. N., Green, S. L., Cotterill, C., Morgan, S., Akizawa, N., ... Zhao, R. (2017). Expedition 357 summary. In G. L. Früh-Green, B. N. Orcutt, S. L. Green, C. Cotterill, and the Expedition 357 Scientists (Eds.), *Atlantis massif serpentinization and life* (pp. 1–34). College Station, TX: International Ocean Discovery Program.
- Früh-Green, G. L., Plas, A., & Dell'Angelo, L. N. (1996). Mineralogical and stable isotope record of polyphase alteration of East Pacific Rise upper crustal gabbros (Hess Deep, Site 894). In *Proceedings-ocean drilling program scientific results* (pp. 235–254). College Station, TX (Ocean Drilling Program): National Science Foundation.

- Garrido, C. J., López-Sánchez-Vizcaíno, V., Gómez-Pugnaire, M. T., Trommsdorff, V., Alard, O., Bodinier, J. L., & Godard, M. (2005). Enrichment of HFSE in chlorite-harzburgite produced by high-pressure dehydration of Antigorite-Serpentinite: Implications for subduction magmatism. *Geochemistry, Geophysics, Geosystems*, 6(1), Q01J15. <https://doi.org/10.1029/2004GC000791>
- Gasc, J., Brunet, F., Brantut, N., Corvisier, J., Findling, N., ... Lathe, C. (2016). Effect of water activity on reaction kinetics and intergranular transport: Insights from the $\text{Ca}(\text{OH})_2 + \text{MgCO}_3 \rightarrow \text{CaCO}_3 + \text{Mg}(\text{OH})_2$ reaction at 1.8 GPa. *Journal of Petrology*, 57(7), 1389–1408. <https://doi.org/10.1093/ptrology/egw044>
- Gómez-Pugnaire, M. T., & Fernández-Soler, J. M. (1987). High-pressure metamorphism in metabasites from the Betic Cordilleras (SE Spain) and its evolution during the Alpine orogeny. *Contributions to Mineralogy and Petrology*, 95(2), 231–244. <https://doi.org/10.1007/BF00381273>
- Gómez-Pugnaire, M., Rubatto, D., Fernández-Soler, J., Jabaloy-Sánchez, A., López-Sánchez-Vizcaíno, V., González-Lodeiro, F., ... Padrón-Navarta, J. (2012). Late Variscan magmatism in the Nevado-Filábride Complex: U-Pb geochronologic evidence for the pre-Mesozoic nature of the deepest Betic complex (SE Spain). *Lithos*, 146, 93–111. <https://doi.org/10.1016/j.lithos.2012.03.027>
- Goscombe, B. D., Passchier, C. W., & Hand, M. (2004). Boudinage classification: End-member boudin types and modified boudin structures. *Journal of Structural Geology*, 26(4), 739–763. <https://doi.org/10.1016/j.jsg.2003.08.015>
- Hatzipanagiotou, K., & Tsikouras, B. (2001). Rodingite formation from diorite in the Samothraki ophiolite, NE Aegean, Greece. *Geological Journal*, 36(2), 93–109. [https://doi.org/10.1002/\(ISSN\)1099-1034](https://doi.org/10.1002/(ISSN)1099-1034)
- Holland, B. T., Blanford, C. F., & Stein, A. (1998). Synthesis of macroporous minerals with highly ordered three-dimensional arrays of spheroidal voids. *Science*, 281(5376), 538–540. <https://doi.org/10.1126/science.281.5376.538>
- Holland, T., & Powell, R. (1996). Thermodynamics of order-disorder in minerals: II. Symmetric formalism applied to solid solutions. *American Mineralogist*, 81(11–12), 1425–1437. <https://doi.org/10.2138/am-1996-11-1215>
- Holland, T. J. B., & Powell, R. (1998). An internally consistent thermodynamic data set for phases of petrological interest. *Journal of Metamorphic Geology*, 16(3), 309–343.
- Holland, T. J. B., & Powell, R. (2011). An improved and extended internally consistent thermodynamic dataset for phases of petrological interest, involving a new equation of state for solids. *Journal of Metamorphic Geology*, 29(3), 333–383. <https://doi.org/10.1111/j.1525-1314.2010.00923.x>
- Honnorez, J., & Kirst, P. (1975). Petrology of rodingites from the equatorial Mid-Atlantic fracture zones and their geotectonic significance. *Contributions to Mineralogy and Petrology*, 49(3), 233–257. <https://doi.org/10.1007/BF00376590>
- Jabaloy-Sánchez, A., Gómez-Pugnaire, M. T., Padrón-Navarta, J. A., López-Sánchez-Vizcaíno, V., & Garrido, C. J. (2015). Subduction-and exhumation-related structures preserved in metaserpentinites and associated metasediments from the Nevado-Filábride Complex (Betic Cordillera, SE Spain). *Tectonophysics*, 644, 40–57. <https://doi.org/10.1016/j.tecto.2014.12.022>
- Jamtveit, B., & Andersen, T. B. (1992). Morphological instabilities during rapid growth of metamorphic garnets. *Physics and Chemistry of Minerals*, 19(3), 176–184.
- Karato, S. I., Wang, Z., Liu, B., & Fujino, K. (1995). Plastic deformation of garnets: Systematics and implications for the rheology of the mantle transition zone. *Earth and Planetary Science Letters*, 130(1–4), 13–30. [https://doi.org/10.1016/0012-821X\(94\)00255-W](https://doi.org/10.1016/0012-821X(94)00255-W)
- Katayama, I., Terada, T., Okazaki, K., & Tanikawa, W. (2012). Episodic tremor and slow slip potentially linked to permeability contrasts at the Moho. *Nature Geoscience*, 5(10), 731. <https://doi.org/10.1038/ngeo1559>
- Katoh, T., & Niida, K. (1983). Rodingites from the Kamuikotan tectonic belt, Hokkaido. *Journal of the Faculty of Science, Hokkaido University, Series 4, Geology and Mineralogy*, 20(2–3), 151–169.
- Kirchner, K. L., Behr, W. M., Loewy, S., & Stockli, D. F. (2016). Early Miocene subduction in the western Mediterranean: Constraints from Rb-Sr multimineral isochron geochronology. *Geochemistry, Geophysics, Geosystems*, 17(5), 1842–1860. <https://doi.org/10.1002/2015GC006208>
- Koutsovitis, P., Magganas, A., Pomonis, P., & Ntaflos, T. (2013). Subduction-related rodingites from East Othris, Greece: Mineral reactions and physicochemical conditions of formation. *Lithos*, 172, 139–157. <https://doi.org/10.1016/j.lithos.2013.04.009>
- Lan, C., & Liou, J. G. (1981). Occurrence, petrology and tectonics of serpentinites and associated rodingites in Central Range, Taiwan. *Memoir of the Geological Society of China*, 4, 343–389.
- Lanari, P., Vidal, O., De Andrade, V., Dubacq, B., Lewin, E., Grosch, E. G., ... Schwartz, S. (2014). XMapTools: A MATLAB®-based program for electron microprobe X-ray image processing and geothermobarometry. *Computers & Geosciences*, 62, 227–240. <https://doi.org/10.1016/j.cageo.2013.08.010>
- Leblanc, M., & Lbouabi, M. (1988). Native silver mineralization along a rodingite tectonic contact between serpentinite and quartz diorite (Bou Azzer, Morocco). *Economic Geology*, 83(7), 1379–1391. <https://doi.org/10.2113/gsecongeo.83.7.1379>
- Li, X.-P., Duan, W.-Y., Zhao, L.-Q., Schertl, H.-P., Kong, F.-M., Shi, T.-Q., & Zhang, X. (2017). Rodingites from the Xigaze ophiolite, southern Tibet-new insights into the processes of rodingitization. *European Journal of Mineralogy*, 29(5), 821–837. <https://doi.org/10.1127/ejm/2017/0029-2633>
- Li, X. H., Putiš, M., Yang, Y. H., Koppa, M., & Dyda, M. (2014). Accretionary wedge harzburgite serpentinization and rodingitization constrained by perovskite U/Pb SIMS age, trace elements and Sm/Nd isotopes: Case study from the Western Carpathians, Slovakia. *Lithos*, 205, 1–14. <https://doi.org/10.1016/j.lithos.2014.06.001>
- Li, X. P., Rahn, M., & Bucher, K. (2004). Metamorphic processes in rodingites of the Zermatt-Saas ophiolites. *International Geology Review*, 46(1), 28–51. <https://doi.org/10.2747/0020-6814.46.1.28>
- Li, X. P., Rahn, M., & Bucher, K. (2008). Eclogite facies metarodingites-phase relations in the system $\text{SiO}_2\text{-Al}_2\text{O}_3\text{-Fe}_2\text{O}_3\text{-FeO-MgO-CaO-CO}_2\text{-H}_2\text{O}$: An example from the Zermatt-Saas ophiolite. *Journal of Metamorphic Geology*, 26(3), 347–364. <https://doi.org/10.1111/j.1525-1314.2008.00761.x>
- Li, X. P., Zhang, L., Wei, C., Ai, Y., & Chen, J. (2007). Petrology of rodingite derived from eclogite in western Tianshan, China. *Journal of Metamorphic Geology*, 25(3), 363–382. <https://doi.org/10.1111/j.1525-1314.2007.00700.x>
- Locock, A. J. (2008). An Excel spreadsheet to recast analyses of garnet into end-member components, and a synopsis of the crystal chemistry of natural silicate garnets. *Computers & Geosciences*, 34(12), 1769–1780. <https://doi.org/10.1016/j.cageo.2007.12.013>

- Locock, A. J. (2014). An Excel spreadsheet to classify chemical analyses of amphiboles following the IMA 2012 recommendations. *Computers & Geosciences*, *62*, 1–11. <https://doi.org/10.1016/j.cageo.2013.09.011>
- López-Sánchez-Vizcaíno, V., Gómez-Pugnaire, M. T., Garrido, C. J., Padrón-Navarta, J. A., & Mellini, M. (2009). Breakdown mechanisms of titanclinohumite in antigorite serpentinite (Cerro del Almirez massif, S. Spain): A petrological and TEM study. *Lithos*, *107*(3–4), 216–226. <https://doi.org/10.1016/j.lithos.2008.10.008>
- López-Sánchez-Vizcaíno, V., Rubatto, D., Gómez-Pugnaire, M. T., Trommsdorff, V., & Müntener, O. (2001). Middle Miocene high-pressure metamorphism and fast exhumation of the Nevado-Filábride Complex, SE Spain. *Terra Nova*, *13*(5), 327–332. <https://doi.org/10.1046/j.1365-3121.2001.00354.x>
- López-Sánchez-Vizcaíno, V., Trommsdorff, V., Gómez-Pugnaire, M. T., Garrido, C. J., Müntener, O., & Connolly, J. (2005). Petrology of titanian clinohumite and olivine at the high-pressure breakdown of antigorite serpentinite to chlorite harzburgite (Almirez Massif, S. Spain). *Contributions to Mineralogy and Petrology*, *149*(6), 627–646. <https://doi.org/10.1007/s00410-005-0678-3>
- Malaspina, N., Langenhorst, F., Tumiati, S., Campione, M., Frezzotti, M. L., & Poli, S. (2017). The redox budget of crust-derived fluid phases at the slab-mantle interface. *Geochimica et Cosmochimica Acta*, *209*, 70–84. <https://doi.org/10.1016/j.gca.2017.04.004>
- Marchesi, C., Garrido, C. J., Padrón-Navarta, J. A., López-Sánchez-Vizcaíno, V., & Gómez-Pugnaire, M. T. (2013). Element mobility from seafloor serpentinization to high-pressure dehydration of antigorite in subducted serpentinite: Insights from the Cerro del Almirez ultramafic massif (southern Spain). *Lithos*, *178*, 128–142. <https://doi.org/10.1016/j.lithos.2012.11.025>
- Massonne, H. J., & Willner, A. P. (2008). Phase relations and dehydration behaviour of psammopelite and mid-ocean ridge basalt at very-low-grade to low-grade metamorphic conditions. *European Journal of Mineralogy*, *20*(5), 867–879. <https://doi.org/10.1127/0935-1221/2008/0020-1871>
- Menzel, M., Garrido, C. J., López-Sánchez-Vizcaíno, V., Marchesi, C., & Hidas, K. (2017, April). Subduction metamorphism of ophi-carbonates beyond the stability of antigorite: insights into carbonate dissolution vs. decarbonation from the Almirez ultramafic massif (S. Spain). In *EGU general assembly conference abstracts* (vol. 19, p. 9189). European Geosciences Union: Göttingen.
- Merkulova, M., Muñoz, M., Brunet, F., Vidal, O., Hattori, K., Vantelon, D., ... Huthwelker, T. (2017). Experimental insight into redox transfer by iron-and sulfur-bearing serpentinite dehydration in subduction zones. *Earth and Planetary Science Letters*, *479*, 133–143. <https://doi.org/10.1016/j.epsl.2017.09.009>
- Merkulova, M., Muñoz, M., Vidal, O., & Brunet, F. (2016). Role of iron content on serpentinite dehydration depth in subduction zones: Experiments and thermodynamic modeling. *Lithos*, *264*, 441–452. <https://doi.org/10.1016/j.lithos.2016.09.007>
- Mittweide, S. K., & Schandl, E. S. (1992). Rodingites from the Southern Appalachian Piedmont, South-Carolina, USA. *European Journal of Mineralogy*, *4*(1), 7–16. <https://doi.org/10.1127/ejm/4/1/0007>
- Mogessie, A., & Rammilmair, D. (1994). Occurrence of zoned uvarovite-grossular garnet in a rodingite from the Vumba Schist Belt, Botswana, Africa: Implications for the origin of rodingites. *Mineralogical Magazine*, *58*(392), 375–386. <https://doi.org/10.1180/minmag.1994.058.392.03>
- Murzin, V. V., & Shanina, S. N. (2007). Fluid regime and origin of gold-bearing rodingites from the Karabash alpine-type ultrabasic massif, Southern Ural. *Geochemistry International*, *45*(10), 998–1011. <https://doi.org/10.1134/S0016702907100047>
- Newton, R. C., & Haselton, H. T. (1981). *Thermodynamics of the garnet-plagioclase-Al₂SiO₅-quartz geobarometer thermodynamics of minerals and melts* (pp. 131–147). New York, NY: Springer. <https://doi.org/10.1007/978-1-4612-5871-1>
- Normand, C., & Williams-Jones, A. E. (2007). Physicochemical conditions and timing of rodingite formation: Evidence from rodingite-hosted fluid inclusions in the JM Asbestos mine, Asbestos, Quebec. *Geochemical Transactions*, *8*(1), 11. <https://doi.org/10.1186/1467-4866-8-11>
- O'Hanley, D. S. (1996). Rodingites, albitites, and other rocks formed by metasomatism. *Serpentinites. Records of tectonic and petrological history* (pp. 112–126). New York, NY/Oxford: Oxford University Press.
- O'Hanley, D. S., Schandl, E. S., & Wicks, F. J. (1992). The origin of rodingites from Cassiar, British-Columbia, and their use to estimate T and P (H₂O) during serpentinization. *Geochimica et Cosmochimica Acta*, *56*(1), 97–108. [https://doi.org/10.1016/0016-7037\(92\)90119-4](https://doi.org/10.1016/0016-7037(92)90119-4)
- Padrón-Navarta, J. A., Hermann, J., Garrido, C. J., López-Sánchez-Vizcaíno, V., & Gómez-Pugnaire, M. T. (2010). An experimental investigation of antigorite dehydration in natural silica-enriched serpentinite. *Contributions to Mineralogy and Petrology*, *159*(1), 25. <https://doi.org/10.1007/s00410-009-0414-5>
- Padrón-Navarta, J. A., López-Sánchez-Vizcaíno, V., Garrido, C. J., & Gómez-Pugnaire, M. T. (2011). Metamorphic record of high-pressure dehydration of antigorite serpentinite to chlorite harzburgite in a subduction setting (Cerro del Almirez, Nevado-Filábride Complex, Southern Spain). *Journal of Petrology*, *52*(10), 2047–2078. <https://doi.org/10.1093/petrology/egr039>
- Padrón-Navarta, J. A., López-Sánchez-Vizcaíno, V., Hermann, J., Connolly, J. A., Garrido, C. J., Gómez-Pugnaire, M. T., ... Marchesi, C. (2013). Tschermak's substitution in antigorite and consequences for phase relations and water liberation in high-grade serpentinites. *Lithos*, *178*, 186–196. <https://doi.org/10.1016/j.lithos.2013.02.001>
- Padrón-Navarta, J. A., Tommasi, A., Garrido, C. J., & López-Sánchez-Vizcaíno, V. (2012). Plastic deformation and development of antigorite crystal preferred orientation in high-pressure serpentinites. *Earth and Planetary Science Letters*, *349*, 75–86. <https://doi.org/10.1016/j.epsl.2012.06.049>
- Padrón-Navarta, J. A., Tommasi, A., Garrido, C. J., López-Sánchez-Vizcaíno, V. L., Gómez-Pugnaire, M. T., Jabaloy-Sánchez, A., & Vauchez, A. (2010). Fluid transfer into the wedge controlled by high-pressure hydrofracturing in the cold top-slab mantle. *Earth and Planetary Science Letters*, *297*(1–2), 271–286. <https://doi.org/10.1016/j.epsl.2010.06.029>
- Panseri, M., Fontana, E., & Tartarotti, P. (2008). Evolution of rodingitic dykes: Metasomatism and metamorphism in the Mount Avic serpentinites (Alpine Ophiolites, southern Aosta Valley). *Ophioliti*, *33*(2), 165–185.
- Perraki, M., Karipi, S., Rigopoulos, I., Tsikouras, B., Pomonis, P., & Hatzipanagiotou, K. (2010). Grossular/hydrogrossular in rodingites from Othrys Ophiolite (Central Greece): Raman spectroscopy as a tool to distinguish it from vesuvianite. *Scientific Analals, School of Geology, Aristotle University of Thessaloniki*, *99*, 317–322.

- Platt, J. P., Anczkiewicz, R., Soto, J. I., Kelley, S. P., & Thirlwall, M. (2006). Early Miocene continental subduction and rapid exhumation in the western Mediterranean. *Geology*, *34*(11), 981–984. <https://doi.org/10.1130/G22801A.1>
- Pomonis, P., Tsikouras, B., Karipi, S., & Hatzipanagiotou, K. (2008). Rodingite formation in ultramafic rocks from the Koziakas ophiolite, western Thessaly, Greece: Conditions of metasomatic alteration, geochemical exchanges and T-X (CO₂) evolutionary path. *The Canadian Mineralogist*, *46*(3), 569–581. <https://doi.org/10.3749/canmin.46.3.569>
- Puga, E., Nieto, J. M., Díaz de Federico, A. D., Bodinier, J. L., & Morten, L. (1999). Petrology and metamorphic evolution of ultramafic rocks and dolerite dykes of the Betic Ophiolitic Association (Mulhacen Complex, SE Spain): Evidence of eo-Alpine subduction following an ocean-floor metasomatic process. *Lithos*, *49*(1–4), 23–56. [https://doi.org/10.1016/S0024-4937\(99\)00035-3](https://doi.org/10.1016/S0024-4937(99)00035-3)
- Puschign, A. R. (2002). Metasomatic alterations at mafic-ultramafic contacts in Valmalenco (Rhetic Alps, N-Italy). *Schweizerische Mineralogische und Petrographische Mitteilungen*, *82*, 515–536.
- Rossmann, G. R., & Aines, R. D. (1991). The hydrous components in garnets: Grossular-hydrogrossular. *American Mineralogist*, *76*(7–8), 1153–1164.
- Schandl, E. S., O'Hanley, D. S., & Wicks, F. J. (1989). Rodingites in serpentinized ultramafic rocks of the Abitibi greenstone-belt, Ontario. *The Canadian Mineralogist*, *27*(4), 579–591.
- Schandl, E. S., O'Hanley, D. S., Wicks, F. J., & Kyser, T. K. (1990). Fluid Inclusions in rodingite: A geothermometer for serpentinization. *Economic Geology and the Bulletin of the Society of Economic Geologists*, *85*(6), 1273–1276. <https://doi.org/10.2113/jgsecongeo.85.6.1273>
- Suzuki, J. (1954). On the rodingitic rocks within the serpentinite masses of Hokkaido. *Journal of the Faculty of Science, Hokkaido University, Series 4, Geology and Mineralogy*, *8*(4), 419–430.
- Terabayashi, M., & Maruyama, S. (1998). Large pressure gap between the Coastal and Central Franciscan belts, northern and central California. *Tectonophysics*, *285*(1–2), 87–101. [https://doi.org/10.1016/S0040-1951\(97\)00194-7](https://doi.org/10.1016/S0040-1951(97)00194-7)
- Trommsdorff, V., & Evans, B. W. (1974). Alpine metamorphism of peridotitic rocks. *Schweizerische Mineralogische und Petrographische Mitteilungen*, *54*, 334–352.
- Trommsdorff, V., López-Sánchez-Vizcaíno, V., Gomez-Pugnaire, M. T., & Müntener, O. (1998). High pressure breakdown of antigorite to spinifex-textured olivine and orthopyroxene, SE Spain. *Contributions to Mineralogy and Petrology*, *132*(2), 139–148. <https://doi.org/10.1007/s004100050412>
- Tsikouras, B., Karipi, S., & Hatzipanagiotou, K. (2013). Evolution of rodingites along stratigraphic depth in the Iti and Kallidromon ophiolites (Central Greece). *Lithos*, *175*, 16–29. <https://doi.org/10.1016/j.lithos.2013.04.021>
- Tsikouras, B., Karipi, S., Rigopoulos, I., Perraki, M., Pomonis, P., & Hatzipanagiotou, K. (2009). Geochemical processes and petrogenetic evolution of rodingite dykes in the ophiolite complex of Othrys (Central Greece). *Lithos*, *113*(3–4), 540–554. <https://doi.org/10.1016/j.lithos.2009.06.013>
- Tumiati, S., Godard, G., Martin, S., Malaspina, N., & Poli, S. (2015). Ultra-oxidized rocks in subduction mélanges? Decoupling between oxygen fugacity and oxygen availability in a Mn-rich metasomatic environment. *Lithos*, *226*, 116–130. <https://doi.org/10.1016/j.lithos.2014.12.008>
- Ulmer, P., & Trommsdorff, V. (1995). Serpentine stability to mantle depths and subduction-related magmatism. *Science*, *268*(5212), 858–861. <https://doi.org/10.1126/science.268.5212.858>
- White, R. W., Powell, R., & Holland, T. J. B. (2007). Progress relating to calculation of partial melting equilibria for metapelites. *Journal of Metamorphic Geology*, *25*(5), 511–527. <https://doi.org/10.1111/j.1525-1314.2007.00711.x>
- Whitney, D. L., & Evans, B. W. (2010). Abbreviations for names of rock-forming minerals. *American Mineralogist*, *95*(1), 185–187. <https://doi.org/10.2138/am.2010.3371>
- Winkler, H. G. F. (1979). *Petrogenesis of metamorphic rocks* (5th ed., pp. 1–348). Berlin, Heidelberg, New York, NY: Springer-Verlag.
- Zanoni, D., Rebay, G., & Spalla, M. I. (2016). Ocean floor and subduction record in the Zermatt-Saas rodingites, Valtouranche, Western Alps. *Journal of Metamorphic Geology*, *34*(9), 941–961. <https://doi.org/10.1111/jmg.12215>

SUPPORTING INFORMATION

Additional supporting information may be found online in the Supporting Information section at the end of the article.

TABLE S1 Summary of representative microprobe analyses of all minerals for selected samples

FIGURE S1 Representative IR normalised spectra for garnet and diopside showing the occurrence of structurally bounded hydroxyl groups in a Grandite-metarodingite (sample AL14-04-C)

FIGURE S2 Transition at the thin section scale between Grand- and Ep-metarodingite. (a) Scanned image of a complete thin section showing the “patchy” distribution of this transformation and the preservation of a relict garnet vein in the lower part. Dark green areas are rich in late amphibole. The location of micrographs from b is outlined in blue colour. (b) Micrographs of selected areas (with parallel and crossed polars: left and right images, respectively) showing the complete transition from garnet-rich zones, with only incipient transformation into green microaggregates of epidote (1), to zones progressively richer in epidote and diopside (2), and the final transformation to the typical assemblage of Ep-metarodingite with only rare garnet relicts (3). Chlorite is lacking in every zone

TABLE S2 Stable assemblages in the number-labelled fields from pseudosections in Figures 10–12

How to cite this article: Laborda-López C, López-Sánchez-Vizcaíno V, Marchesi C, et al. High-*P* metamorphism of rodingites during serpentinite dehydration (Cerro del Almiraz, Southern Spain): Implications for the redox state in subduction zones. *J Metamorph Geol.* 2018;36:1141–1173. <https://doi.org/10.1111/jmg.12440>